

# **High Efficiency and High Rate Deposited Amorphous Silicon-Based Solar Cells**

## **PHASE II Annual Technical Progress Report**

September 1, 2002 to August 31, 2003

**NREL Subcontract No. NDJ-2-30630-08**

Subcontractor: The University of Toledo

Principal Investigator: Xunming Deng  
Department of Physics and Astronomy  
University of Toledo, Toledo, OH 43606  
(419) 530-4782  
dengx@physics.utoledo.edu

Co-Investigator: Alvin D. Compaan  
Victor Karpov

Contract technical monitor: Dr. Bolko von Roedern

## **Table of Content**

Cover Page

Table of Content

List of Figures

List of Tables

Section 1 Executive Summary

Section 2 High-Efficiency Single-Junction a-SiGe Solar Cells

Section 3 Optimization of High-efficiency a-Si Top Cell

Section 4 Amorphous Silicon Deposited Using Trisilane as Precursor

Section 5 Deposition of a-SiGe:H and nc-SiGe:H films using HWCVD

## List of Figures

Figure 2-1 Schematic of the device showing the p-layer with sublayers deposited at different temperature.

Figure 2-2. J-V curves of a-SiGe cell (GD904-2.32) measured before and after light soaking for 100 and 3300 hours, showing 10.47% stable, active-area efficiency.

Figure 2-3 J-V curve of a single-junction a-SiGe solar cell with initial, active-area efficiency of around 13%.

Figure 3-1. An optimized top cell deposited on Ag/ZnO back reflector, showing 11.1% initial, active-area efficiency.

Figure 3-2 J-V curve of an improved a-Si solar cell showing 1.023 V open circuit voltage and 78% fill factor. The current is such that it is ideal for use as the top cell of a triple cell.

Figure 4-1. Deposition rates of intrinsic a-Si:H film deposited under the conditions of RF power = 25 mW/cm<sup>2</sup> and T<sub>s</sub> = 150°C. Square symbols represent Si<sub>2</sub>H<sub>6</sub> series and diamond symbols represent Si<sub>3</sub>H<sub>8</sub> series; The solid triangles represent the relationship between deposition rates and R<sub>a</sub> = [H]/[Si] for Si<sub>3</sub>H<sub>8</sub> series.

Figure 4-2 Raman spectra of the series of sample deposited using Si<sub>3</sub>H<sub>8</sub> (2a) and Si<sub>2</sub>H<sub>6</sub> (2b). In Fig. 4-2a, curves from bottom to top are for Si:H deposited with R = 143, 179, 213, and 286. In Fig. 4-2b, curves from bottom to top are for a-Si:H deposited with R = 75; 100; 125; and 150.

Figure 4-3 Activation energy of a-Si:H films made using Si<sub>2</sub>H<sub>6</sub> and Si<sub>3</sub>H<sub>8</sub> as a function of hydrogen dilution R.

Figure 4-4 Microstructure factor R\* as a function of hydrogen dilution R.

Figure 4-5 H content estimated from FTIR spectra as a function of H<sub>2</sub> dilution R

Figure 4-6 Photosensitivity of a-Si:H films deposited using Si<sub>2</sub>H<sub>6</sub> and Si<sub>3</sub>H<sub>8</sub> as a function of hydrogen dilution.

Figure 4-7 Open circuit voltage versus H<sub>2</sub> dilution for Si<sub>2</sub>H<sub>6</sub> and Si<sub>3</sub>H<sub>8</sub> devices.

Figure 5-1 Dependence of the deposition rate  $r_{\text{dep}}$  on the filament temperature  $T_{\text{fil}}$  and the substrate Temperature  $T_{\text{sub}}$  at a Si<sub>2</sub>H<sub>6</sub> flow rate  $F_{\text{Si2H6}} = 3.4$  sccm, GeH<sub>4</sub> flow rate  $F_{\text{GeH4}} = 1.7$  sccm, H<sub>2</sub> flow rate  $F_{\text{H2}} = 7.0$  sccm, a total process pressure  $p = 3.1$  mtorr.

Figure 5-2 Top-view SEM images of SiGe samples deposited at a Si<sub>2</sub>H<sub>6</sub> flow rate  $F_{\text{Si2H6}} = 3.4$  sccm, GeH<sub>4</sub> flow rate  $F_{\text{GeH4}} = 1.7$  sccm, H<sub>2</sub> flow rate  $F_{\text{H2}} = 7.0$  sccm, a total process pressure  $p =$

3.1 mtorr using a)  $T_{\text{fil}} = 1800\text{ }^{\circ}\text{C}$  and  $T_{\text{sub}} = 200^{\circ}\text{C}$ , b)  $T_{\text{fil}} = 1800\text{ }^{\circ}\text{C}$  and  $T_{\text{sub}} = 300^{\circ}\text{C}$ , c)  $T_{\text{fil}} = 2000\text{ }^{\circ}\text{C}$  and  $T_{\text{sub}} = 200^{\circ}\text{C}$ , and d)  $T_{\text{fil}} = 2000\text{ }^{\circ}\text{C}$  and  $T_{\text{sub}} = 300^{\circ}\text{C}$ .

Figure 5-3 Raman spectra of SiGe and Ge films deposited with different  $T_{\text{fil}}$ ,  $T_{\text{sub}}$  and gas mixtures.

Figure 5-4 The GID X-ray spectrum of the SiGe film deposited at  $F_{\text{Si}_2\text{H}_6} = 3.4\text{ sccm}$ ,  $F_{\text{GeH}_4} = 1.7\text{ sccm}$ ,  $F_{\text{H}_2} = 7.0\text{ sccm}$ ,  $p = 2.5\text{ mTorr}$ ,  $T_{\text{sub}} = 200\text{ }^{\circ}\text{C}$  and  $T_{\text{fil}} = 1800^{\circ}\text{C}$  for 10 min with a film thickness of  $d = 141\text{ nm}$ .

Figure 5-5 Raman and FTIR spectra of SiGe films deposited at  $F_{\text{Si}_2\text{H}_6} = 3.4\text{ sccm}$ ,  $F_{\text{GeH}_4} = 1.7\text{ sccm}$ ,  $F_{\text{H}_2} = 7.0\text{ sccm}$ ,  $p = 3.1\text{ mTorr}$ ,  $T_{\text{sub}} = 200\text{ }^{\circ}\text{C}$  and  $T_{\text{fil}} = 1800^{\circ}\text{C}$  for 15 min using filament Type S.

## **List of Tables**

Table 2-1. Deposition conditions and device performance for a series of a-SiGe solar cells having bandgap optimal for use in high-efficiency single-junction solar cells.

Table 2-2 Performance of a-SiGe solar cells deposited using p-layers deposited at different temperature or different combination of temperatures.

Table 3-1 Deposition conditions and J-V performance for a series of a-Si solar cells.

Table 4-1. Volume fraction of nanocrystalline silicon phase estimated from Raman spectra for two series of sample. Thicknesses of samples are also included in the Table.

Table 5-1: The parameters of the coil-shaped filament used in this study.

## Section 1 Executive Summary

This report covers the second year of this subcontract for research on High Efficiency and High-Rate Deposited Amorphous Silicon-Based Solar Cells, under subcontract number NDJ-1-30630-08. The period of performance covered by this report is September 1, 2002 to August 31, 2003.

Following this Executive Summary are four sections performed during each of the four quarters. The subjects of these four sections are:

- Section 2 High-Efficiency Single-Junction a-SiGe Solar Cells
- Section 3 Optimization of High-efficiency a-Si Top Cell
- Section 4 Amorphous Silicon Deposited Using Trisilane as Precursor
- Section 5 Deposition of a-SiGe:H and nc-SiGe:H films using HWCVD

In the following, we summarize the activities related to each of the seven tasks under this subcontract.

Task 1: Grand phase diagram for deposition of protocrystalline Si and SiGe materials.

During the last year, we studied the phase diagram for a-Si deposition for different H dilution and substrate temperature  $T_s$ . In order to be able to cover a broader parameter space within a limited time, we designed and installed a load lock chamber that allows us to load in simultaneously a set of ten 4"x4" masks with different patterns of coverage for the deposition. In this way, we could explore a large set of parameters in a single vacuum pump down. We have also studied the deposition of protocrystalline Si and SiGe using rf PECVD and HWCVD during this program period.

Task 2: Deposition of a-Si based materials using new gas precursors

A systematic study of Si:H deposition using  $\text{Si}_3\text{H}_8$  and  $\text{Si}_2\text{H}_6$  was performed, with the results summarized in Section 4. In this study, Si:H films and solar cells deposited using  $\text{Si}_3\text{H}_8$  and using  $\text{Si}_2\text{H}_6$  are compared. At the same hydrogen dilution,  $\text{Si}_3\text{H}_8$  leads to higher deposition rate. However, at the same atomic ratio of hydrogen and silicon, the deposition rate of Si:H using  $\text{Si}_3\text{H}_8$  and  $\text{Si}_2\text{H}_6$  is approximately the same. The deposition rate is more influenced by the ratio of the total number of Si atoms to hydrogen atoms introduced into the chamber rather than the number of Si-containing molecules. Measurement of activation energy, microstructure and photosensitivity indicate that 1) the transition from amorphous to amorphous/nanocrystalline mixed phase occurs at a higher hydrogen dilution level when  $\text{Si}_3\text{H}_8$  is used; and 2) the transition from amorphous to mixed phase is more gradual for  $\text{Si}_3\text{H}_8$  as compared with  $\text{Si}_2\text{H}_6$ . This suggests that the window of parameter space for deposition of high-quality protocrystalline silicon may be wider when  $\text{Si}_3\text{H}_8$  is used as compared with  $\text{Si}_2\text{H}_6$  and  $\text{SiH}_4$ .

Task 3: Study of nanometer-sized doped layers and the band-edge mismatch at hetero-interfaces

In this task area, we studied nanometer-sized p-layer that forms a desirable hetero-interface with the intrinsic absorber layer and yet has minimal optical absorption. A multiple-sublayer approach is used to meet these two requirements simultaneously. Using such a multiple-sublayered nanometer-sized p-layer, we achieved single-junction a-SiGe solar cells with initial efficiency approximately 12.5% and stabilized efficiency of 10.5% (not yet independently confirmed). A US utility patent application was filed for the p-layer concept. Results of this study are summarized in Section 2.

In addition, we have nearly completed the installation and optimization of a 5-chamber addition to UT's existing four-chamber PECVD/HWCVD systems. Four of the five chambers are used for the sputter deposition of metal (Al, Ag, etc), ZnO, ITO, SiO<sub>2</sub> layers and the fifth one is a new load-lock chamber capable of simultaneously loading 10 substrates, marks, or combinations of substrates and masks. This system allows us to complete the entire 12 layers of a triple-junction solar cell, Al/ZnO/nip/nip/nip/ITO in a single vacuum pump down, thus avoiding the undesirable air exposure at some of the critical interfaces. The ability to control the air exposure at these interfaces could lead us to understand and analyze the optical and electrical losses at these interfaces such as ZnO/n and p-ITO interfaces. The design and the process optimization of these five new chambers is supported by this NREL-funded project while the acquisition of components and the installation are supported by a complementary project funded by Air Force Research Lab.

#### Task 4: Fabrication of triple-junction cells

Activities in this task area is mostly focused on 1) the optimization of top component cell, as summarized in Section 3; 2) the optimization of the sputter deposition of ITO, Al, ZnO in the new deposition system; 3) the generation of metal fingers using lithography; and 4) deposition of triple-junction a-Si based solar cells.

#### Task 5: Technique for measuring component cell I-V in a two-terminal triple stack

Work in this area is continued during Phase II.

#### Task 6: Modeling of triple-junction cells with AMPS and comparison with fabricated devices.

Work in this area is continued during Phase II.

#### Task 7: High-rate deposition of a-Si based solar cells

Under this task area, we continued our study of the deposition of Si:H materials using HWCVD and VHF PECVD. In the HWCVD area, we studied the effect of the Si:H growth on different filament geometry. We also studied SiGe:H materials with different Ge content in the film and the deposition of amorphous and nanocrystalline SiGe:H alloys using different amounts of hydrogen dilution. Some of the studies in this area are summarized in Section 5. In the VHF PECVD area, new matching box was installed. The modification of hardware allows us to incorporate more power into the plasma and leads to higher deposition rate. Study of the deposition uniformity was also carried out. It was found that the film uniformity is the highest when the chamber pressure was kept near 0.35 Torr in our deposition system.

## Section 2 High-Efficiency Single-Junction a-SiGe Solar Cells

Contributors: W. Du, X. Yang, H. Povolny and X. Deng

### ABSTRACT

Single-junction a-SiGe solar cells were fabricated using plasma enhanced chemical vapor deposition on stainless steel substrate coated with Ag/ZnO back-reflector. Incorporating 1) an optimized a-SiGe i-layer with thickness and bandgap more suitable for single-junction cell, and 2) a hybrid p-layer with the sub-layer near a-SiGe i-layer deposited at a relatively high temperature for an optimal p-i interface and the bulk of the p-layer deposited at a relatively lower temperature for a better transparency, we achieved single-junction a-SiGe solar cells with initial, active-area efficiency greater than 12.5% and stable, active-area efficiency of 10.4%. Such high efficiency single-junction solar cells have important applications since they have initial and stabilized efficiencies approaching those usually obtainable with a multiple-junction structure, yet can be fabricated using a much simpler deposition process.

### INTRODUCTION

We have previously reported our optimization of medium bandgap a-SiGe solar cell for use as the middle component cell of a triple-junction solar cell. In order to fabricate high efficiency single-junction solar cell which is simpler to manufacture, an ideal bandgap is close to that of the middle cell but not necessary the same. In this work, we investigated medium bandgap a-SiGe solar cell toward achieving single-junction solar cells with highest stable efficiency.

In our earlier work, we also reported the stability test of single-junction a-SiGe devices with different Ge in the i-layer. It was surprising to find a-SiGe cells with small amount of Ge in the i-layer were more stable than a-Si cell without Ge in the i-layer after light soaking. It is for this reason, we expect to fabricate single-junction a-SiGe cells with higher stabilized efficiency than single-junction a-Si cells.

In terms of p-layer fabrication, we reported previously that high performance wide bandgap single-junction a-Si solar cells ( $V_{oc}=1.014V$  and  $FF=74.6\%$ ) were obtained using p-layer deposited near the transition region between nanocrystalline silicon (nc-Si) and a-Si at a low temperature ( $T_s = 70\text{ C}$ ). However, when such a p-layer, ideal for wide bandgap a-Si top cell, is used for narrow bandgap a-SiGe bottom cell in a multiple-junction solar cell, severe roll-over occurs in the J-V curve, possibly due to a mismatch at the p-i interface. It was further discovered that p-layer deposited at a higher  $T_s$  (140 C) forms a good interface with NBG a-SiGe i-layer and leads to ideal J-V curve [1]. The diode characteristics is even better than that of top cell. However, this p-layer, p ( $T_s=140C$ ), is less transparent than p ( $T_s=70C$ ). Although it is acceptable for use in middle and bottom component cell in a triple stack, it is not acceptable for use as the window layer in any single-junction solar cell.



## APPROACH

### Intrinsic Layer Optimization

We start with a-SiGe medium bangap cell used as the middle cell inside a triple-junction stack and adjust the bandgap (i.e., Si:Ge ratio) and the thickness while maintaining the hydrogen dilution to be near the transition region from amorphous to microcrystalline.

### Doped Layer Optimization

To obtain a p-layer that forms good interface with a-SiGe and is more transparent as the window layer, we explored the use of a hybrid, stacked p-layer with sublayers deposited at  $T_s=140^\circ\text{C}$  and  $70^\circ\text{C}$  [2], as depicted in Figure 2-1.

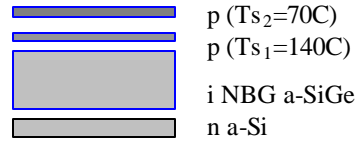


Figure 2-1 Schematic of the device showing the p-layer with sublayers deposited at different temperature.

## EXPERIMENTAL

The structure of single-junction a-SiGe solar cell fabricated in this study is SS/Ag/ZnO/ $n^+$ /n/b/a-SiGe-i/b/ $p^+$ /ITO, where SS is stainless steel foil substrate,  $p^+$  and  $n^+$  are heavily doped interface layers, and /b/ on both sides of a-SiGe i-layers are bandgap graded buffer layers. All of the semiconductor layers were deposited using University of Toledo (UT)'s multiple-chamber PECVD system. The substrate coated SS is provided by Energy Conversion Devices, Inc. (ECD) and United Solar. ITO is deposited at UT using rf sputtering from a ITO target in Ar ambient. The solar cells were characterized at UT using a Xe-lamp solar simulator and a quantum efficiency measurement system Detailed description of the experimental details can be found in our earlier reports [3].

Thickness of the nip cells were measured using reflection measurement from interference peaks of the actual device. Therefore, the thickness used here is the combined thickness of n,i,p layers rather than that of the i-layer.

## RESULTS

### Optimization of the i-layer

Table 2-1 shows the results of a series of a-SiGe solar cells having a structure of SS/ $n^+$ /n/b/a-SiGe-i/b/ $p^+$ /ITO (for GD830, GD895, GD896, GD897) or SS/Ag/ZnO/ $n^+$ /n/b/a-SiGe-i/b/ $p^+$ /ITO (for GD905). GD895 is deposited under our standard middle cell condition, used for the fabrication of triple cells with 12.7% initial efficiency. Device GD895, 896, 897 incorporate increasingly more

$\text{Si}_2\text{H}_6$  in the gas mixture, results in increasingly higher bandgap. The i-layer of device GD897 is deposited in 40 min while the rest of the devices in 60 min. It is expected we see increasingly higher  $V_{oc}$  when  $\text{Si}_2\text{H}_6$  is increased, the higher  $J_{sc}$  is due to the increased i-layer thickness. In the table, the thickness of nip was calculated from interference fringes in the reflection spectra. There is no obvious drop in the FF, at least in the initial state, when the i-layer is made with more  $\text{Si}_2\text{H}_6$  (less Ge and thicker). Sample GD905 was made with a bandgap-graded a-SiGe i-layer so that the bandgap near the p-layer is smaller. In this way, more light is absorbed near the p-layer so that holes has less distance to travel to the p-layer and get collected. However, there is a significant drop in the open circuit voltage, which seems to be governed by the narrowest point in the i-layer bandgap, rather than the average bandgap. Sample GD905 shows higher efficiency since it is deposited on back-reflector. The thickness of GD905 is not provided since it is deposited on a texture back reflector which prevents us from using interference fringes to calculate the thickness.

Since GD895 shows the highest FF, in addition to higher  $V_{oc}$  and  $J_{sc}$ , it is selected for use as the standard i-layer deposition condition for single-junction a-SiGe cells.

We performed light soaking stability test. The light soaking was done using metal halide lamp with  $100 \text{ mW/cm}^2$  light intensity. The samples are maintained at a temperature near  $50^\circ\text{C}$ . Figure 2-2 shows the J-V curve of one cell in GD904, deposited under the same conditions as GD895, but on Ag/ZnO back reflector. The initial cell efficiency is 12.1%. After 100 and 3300 hours of light soaking, the stabilized efficiency is 10.5%. This is, to the best of our knowledge, highest reported stabilized efficiency for a single-junction a-Si based solar cell.

Table 2-1. Deposition conditions and device performance for a series of a-SiGe solar cells having bandgap optimal for use in high-efficiency single-junction solar cells

sample	$\text{Si}_2\text{H}_6$	$\text{GeH}_4$	$\text{H}_2$	Time	d of nip	$V_{oc}$	$I_{sc}$	FF	Eff	Substrate
No	(sccm)	(sccm)	(sccm)	(min)	(nm)	(V)	(mA/cm <sup>2</sup> )	(%)	(%)	
gd830	1.5	2.75	100	60	323	0.830	14.2	70.2	8.7	SS
gd895	2	2.75	100	60	271	0.861	15.6	70.8	9.5	SS
gd896	2.5	2.75	100	60	382	0.873	16.0	69.4	9.7	SS
gd897	3	2.75	100	40	300	0.886	14.2	72.7	9.1	SS
gd905	2	1.8-3.8	100	60		0.833	20.7	68.1	11.8	BR

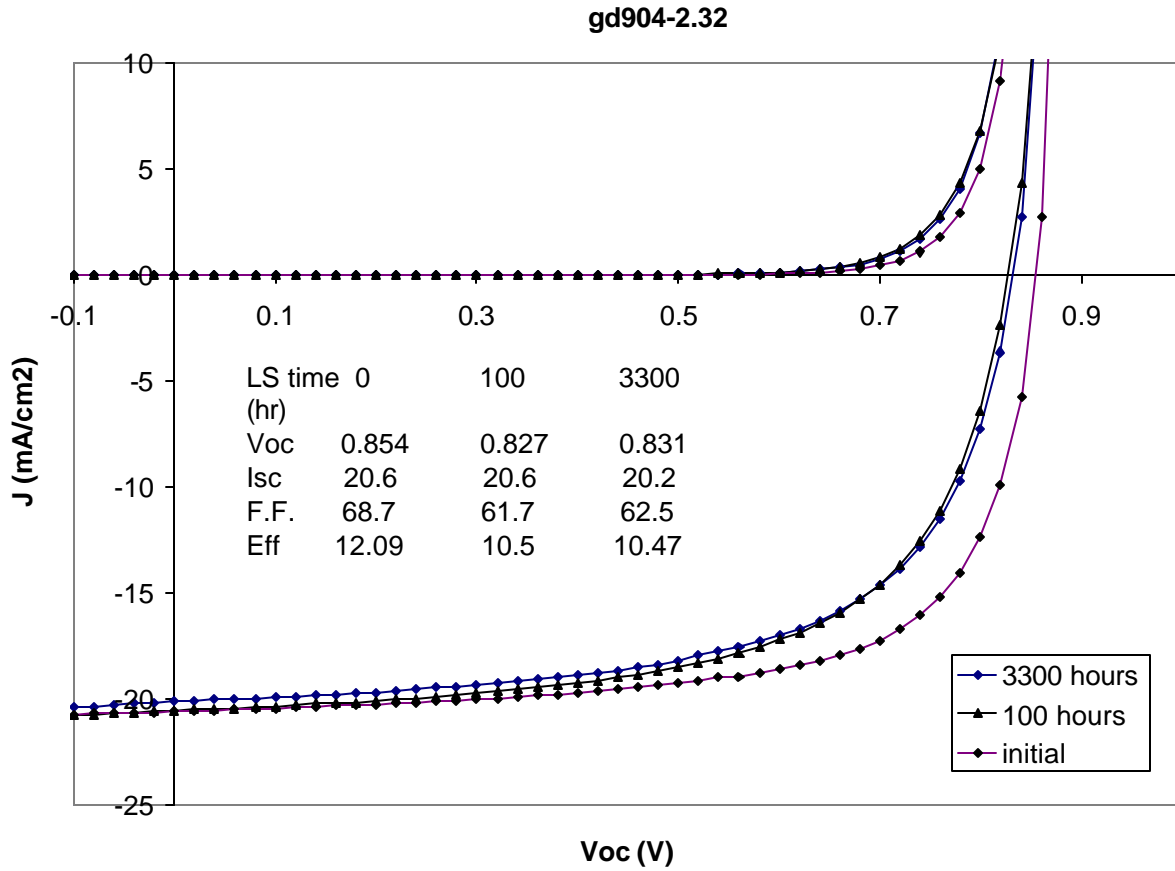


Figure 2-2. J-V curves of a-SiGe cell (GD904-2.32) measured before and after light soaking for 100 and 3300 hours, showing 10.47% stable, active-area efficiency.

### Optimization of the p-layer

Using the i-layer for GD895 (or GD904 which has the same i-layer), we fabricate a series of a-SiGe single-junction solar cells with different p-layers. Boron doped layers, deposited at different temperatures, are used for the window layer. In Table 2-2, we present a series of devices with p-layer deposited at: 1) only 140 C, which is the temperature for all samples shown in Table 2-1; 2) only 70 C, which is the ideal temperature for p-layer used in our high-efficiency top cells, 3) both 140 C (for time  $t_1$ ) and 70 C (for time  $t_2$ ). Again, GD904 is the standard condition as a reference. It is found that the device (GD919) with p-layer deposited at a higher temperature for a relative short time ( $t_1=1\text{min}$ ) and a lower temperature for a relatively longer time ( $t_2=2\text{min}$ ) forms a good interface with the narrow bandgap a-SiGe layer, as reflected in the high FF, and is more transparent, as reflected in the high Jsc. Figure 2-3 shows the J-V curve of one cell in GD919 showing an initial, active-area efficiency of 12.8% ( $V_{oc}=0.843\text{ V}$ ,  $FF=0.727$  and  $J_{sc}=21.3\text{ mA/cm}^2$ ). We think the current density might be slightly overestimated by a few percent according to quantum efficiency measured. We performed light soaking test for these cells for these samples. After 100 hours of light soaking, these samples with double p-layer show 10.4% stable efficiency. More light soaking test is

to be performed. We believe that the improved  $J_{sc}$  due to the p-layer should not alter the light soaking stability.

Table 2-2 Performance of a-SiGe solar cells deposited using p-layers deposited at different temperature or different combination of temperatures

Sample	$t_1$ (min)	$t_2$ (min)	Voc	$J_{sc}$	FF	$\eta$
No	140C	70C	(V)	(mA/cm <sup>2</sup> )	(%)	(%)
GD904	3	0	0.856	20.6	68.6	12.1
GD907	0	3	0.856	20.7	65.9	11.7
GD908	0.5	2	0.858	21.0	66.9	12.1
GD919	1	2	0.847	21.5	70.1	12.8

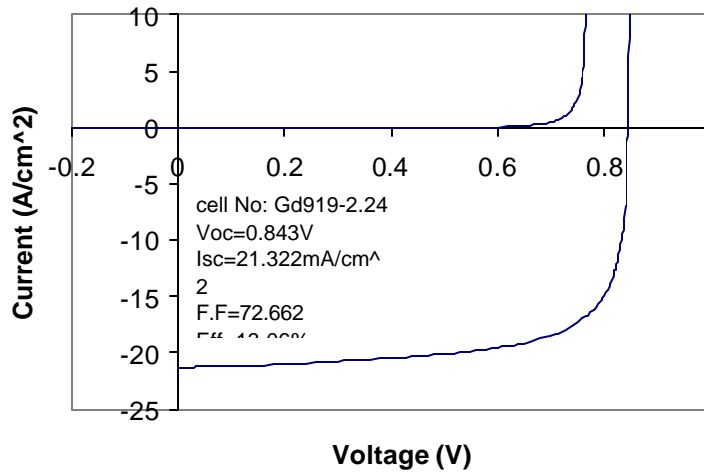


Figure 2-3 J-V curve of a single-junction a-SiGe solar cell with initial, active-area efficiency of around 13%.

## SUMMARY

High-efficiency single-junction a-SiGe solar cells are obtained using 1) improve a-SiGe i-layer and 2) a p-layer deposited with two separate steps: with one at a higher temperature for better interface with a-SiGe i-layer and the other at a lower temperature for better transmission. We achieved a-SiGe single-junction cells with greater than 12.5% initial, active-area efficiency and 10.4% stabilized efficiency.

## ACKNOWLEDGEMENTS

We would like to thank researchers at ECD, United Solar, NREL and UT CdTe group for collaborations and assistance. Research assistance from and discussions with X. Liao, W. Wang, X. Xiang are particularly appreciated.

## REFERENCES

- [1] X. Liao, W. Wang, and X. Deng, Proc. of 29<sup>th</sup> IEEE PVSC, 1234 (2001).
- [2] X. Liao et al, to be submitted to Proc. of 3<sup>rd</sup> WCPEC (2003).
- [3] W. Wang, H. Povolny, W. Du, X. Liao and X. Deng, Proc. of 29<sup>th</sup> IEEE PVSC, 1082 (2001).

## Section 3 Optimization of High-efficiency a-Si Top Cell

Contributors: W. Du, X. Yang and X. Deng

### Introduction

In this study, we optimize the deposition of a-Si cell for use as top component cell inside a triple-junction stack. In addition, we optimize the solar cell for use as a single-junction a-Si solar cell without any Ge in the i-layer. Third, we explore the possibility of improving the p-layer using a double-p-layer deposited at different temperatures, which lead to significant improvement in the performance of medium bandgap a-SiGe cells.

### Experimental

Amorphous Si solar cells having a structure of SS/Ag/ZnO/n<sup>+</sup>/n/a-Si-i/p/p<sup>+</sup>/ITO or SS/n<sup>+</sup>/n/a-Si-i/p/p<sup>+</sup>/ITO are deposited using a PECVD system with all three types of layers deposited in separated PECVD chambers. The p-layers are deposited in two different steps at different temperatures for some of the samples.

### Results

Table 3-1 shows the performance for a series of a-Si cells deposited with different SiH<sub>4</sub> and H<sub>2</sub> flows and different i-layer deposition times. In addition, two samples, GD909 and GD912 are deposited with a p-layer deposited in two steps. From Table 3-1, we observe the following:

- Comparing GD921 and GD915, thicker i-layer leads to higher J<sub>sc</sub> and lower FF, while Voc is unchanged.
- Comparing GD915 and GD910, less dilution and short time leads to device with higher FF.
- Two-step p-layer does not show improvement for the top cell.
- Sample deposited with a graded hydrogen dilution, with intent to keep the structure of a-Si on the amorphous side without becoming microcrystalline, does not show any improvement. This is puzzling and should be repeated in the future.
- Sample with intermediate H dilution (H<sub>2</sub>/SiH<sub>4</sub>=100/1.5) exhibit highest initial efficiency.

Figure 3-1 shows the JV curve of GD912, showing 11.1% initial efficiency. We have later further improve the fabrication process such as the ITO layers. This results in a further improvement in the cell performance. Figure 3-2 shows an improved cell, ideal for use as an top component, showing 1.023 V open circuit voltage and 78% fill factor.

Table 3-1 Deposition conditions and J-V performance for a series of a-Si solar cells

Sample	Si2H6	H2	t(i-layer)	t (p-layer)	Voc	Jsc	FF	Eff	Substrate
No.	(min)			(min)	(V)	(mA/cm <sup>2</sup> )	(%)	(%)	
				140C/70C					
gd909	1	100	60	1/2	0.988	13.2	72.0	9.36	Ag/ZnO
gd921	1	100	60	0/4	0.986	9.2	71.2	6.48	SS
gd915	1	100	120	0/4	0.982	11.3	66.7	7.62	SS
gd910	2	100	60	0/4	0.961	11.9	69.5	7.98	SS
gd911	2	100	40	0/3	0.949	10.9	71.2	7.37	SS
gd912	1.5	100	60	1/3	0.968	11.0	71.1	7.58	SS
gd914	1	75	120	0/4	0.982	17.4	65.3	11.15	Ag/ZnO
gd917	1	100-50	60	0/3	0.957	11.8	64.5	7.26	SS

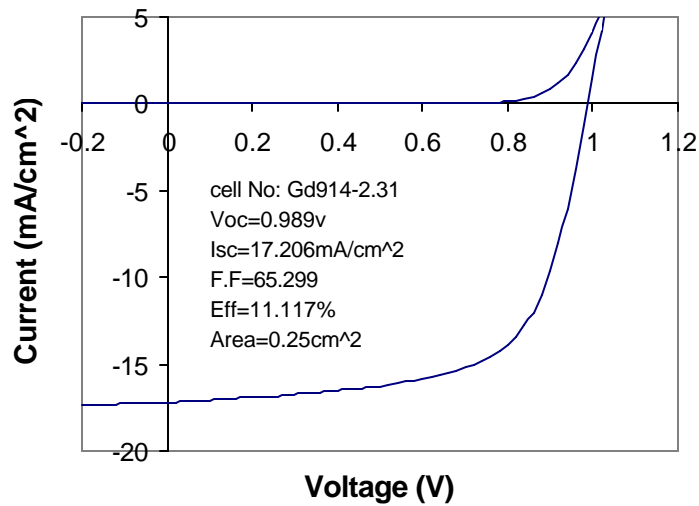


Figure 3-1. An optimized top cell deposited on Ag/ZnO back reflector, showing 11.1% initial, active-area efficiency.

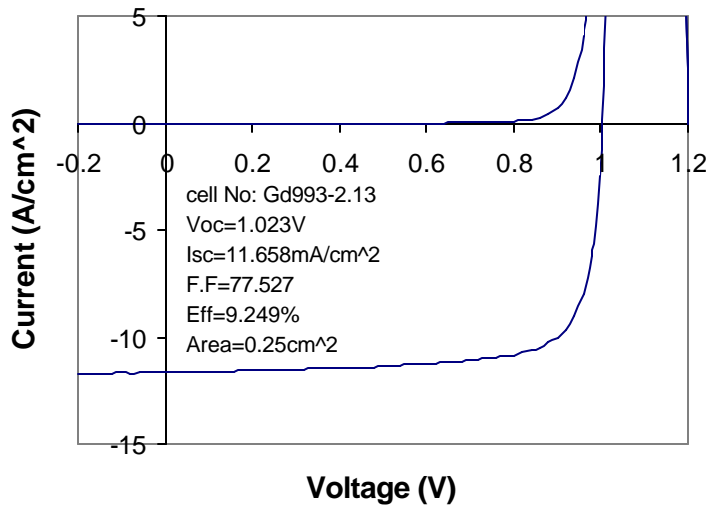


Figure 3-2 J-V curve of an improved a-Si solar cell showing 1.023 V open circuit voltage and 78% fill factor. The current is such that it is ideal for use as the top cell of a triple cell.

## Summary

We optimized a-Si solar cell i-layer and p-layer and obtained improved top cell:

- Wide bandgap a-Si top cell with 11.1% initial efficiency
- Wide bandgap a-Si top cell with 1.023V Voc and 78% FF



## Section 4 Amorphous Silicon Deposited Using Trisilane as Precursor

Contributors:

W. Du, X. Yang and X. Deng, UT

Mike Pikulin and John de Neufville, Voltaix.

### Abstract

We explored the deposition of hydrogenated amorphous silicon (a-Si:H) and hydrogenated nanocrystalline silicon (nc-Si:H) using trisilane ( $\text{Si}_3\text{H}_8$ ) gas as the silicon precursor in a plasma enhanced CVD process, to improve our understanding of the growth chemistry and the dependence of Si:H properties on the use of precursors. The film study shows that the transition from amorphous to amorphous/nanocrystalline mixed phase with increasing hydrogen dilution  $R$  ( $([\text{H}_2]/[\text{Si}_3\text{H}_8])$  or  $([\text{H}_2]/[\text{Si}_2\text{H}_6])$ ) is more gradual for  $\text{Si}_3\text{H}_8$ -deposited Si:H as compared with disilane ( $\text{Si}_2\text{H}_6$ ) deposited Si:H and for the former the transition occurs at a higher hydrogen dilution level  $R$ . The deposition rate of Si:H with different hydrogen dilution is more dependent on the atomic ratio of H to Si rather than the ratio of molecular hydrogen and silicon-containing precursors. Open circuit voltages ( $V_{oc}$ ) of a-Si:H single-junction n-i-p solar cells versus hydrogen dilution is used as a measure of nanocrystalline formation in the i-layer. Highest  $V_{oc}$  is obtained when a-Si:H films are deposited using  $\text{Si}_3\text{H}_8$  at  $R \sim 200$  while highest  $V_{oc}$  is obtained for  $\text{Si}_2\text{H}_6$  at  $R \sim 100$ .

### Introduction

Various silicon precursors, including  $\text{SiH}_4$ ,  $\text{Si}_2\text{H}_6$ ,  $\text{SiF}_4$ , and  $\text{SiH}_2\text{Cl}_2$ , have been used for the deposition of a-Si:H (or a-Si) in a plasma enhanced chemical vapor deposition (PECVD, rf 13.56 MHz) process. Among these different precursors,  $\text{SiH}_4$  and  $\text{Si}_2\text{H}_6$  were found to produce a-Si:H materials with the highest photovoltaic quality. Compared with  $\text{SiH}_4$ ,  $\text{Si}_2\text{H}_6$  has higher dissociation rate in plasma and results in different concentrations of reactive species such as  $\text{SiH}_3$  in the plasma. Such a different concentrations of reactive  $\text{SiH}_3$  species, believed to be responsible for the growth of high quality a-Si:H, leads to different deposition rate and different optimal level of hydrogen dilution for the growth of high quality a-Si:H.

When these silicon precursors are sufficiently diluted in hydrogen during PECVD process, nc-Si:H (or nc-Si), having grain size in the order of magnitude of 10nm, is often obtained. In the intermediate level of hydrogen dilution, a mixed phase with coexisting a-Si:H and nc-Si:H is usually obtained where nanometer sized Si crystals remain embedded in amorphous Si matrix. It is generally found that a-Si:H with highest stability under extended light illumination accompanied with reasonably high photosensitivity is often obtained at a hydrogen dilution level right below the transition from amorphous to mixed phase. A-Si:H deposited under these conditions are often referred to as “protocrystalline Si”, or “edge Si” materials. The range of optimal hydrogen dilution for the deposition of high-quality protocrystalline Si depends on the selection of Si precursor and other deposition conditions and is generally quite narrow. It also changes with the thickness of the a-Si:H film as well as the types of substrates. The sharp nature of transition region hinders reproducibility of the materials deposited within. It is desirable to

have a silicon precursor that offers a wider range of hydrogen dilution for the deposition of high quality protocrystalline Si material.

Trisilane,  $\text{Si}_3\text{H}_8$ , is another member of the silicon-hydrogen compound gasses. It has a different dissociation rate than  $\text{SiH}_4$  and  $\text{Si}_2\text{H}_6$  in an rf plasma. It is expected that  $\text{Si}_3\text{H}_8$  could lead to a higher concentration of  $\text{SiH}_3$  species in plasma when the gas is diluted in appropriate amount of hydrogen. This may lead to higher quality a-Si:H and/or wider window for the deposition of high quality a-Si:H. A systematic study of  $\text{Si}_3\text{H}_8$  deposition of Si:H could lead to a deeper understanding of the nature of transition from amorphous to mixed and finally to nanocrystalline phase of Si:H during PECVD growth under high hydrogen dilution. Such a study may also lead to a-Si:H material with improved stability under extended illumination. In this work, the growth of Si:H near the transition region using  $\text{Si}_3\text{H}_8$  and  $\text{Si}_2\text{H}_6$  as the precursor gasses is studied. This comparative study is carried out by depositing and characterizing both single layer undoped films and solar cell devices.

## Experiment details

Trisilane is a pyrophoric liquid. For PECVD or CVD applications it can be supplied as a gas mixture or as the pure liquid. Due to its low vapor pressure (approximately 250 T at room temperature), for any large volume application, liquid packaging is required. This normally involves a conventional MOCVD "bubbler", essentially a container with a "dip-tube" – a tube immersed in the liquid - and two valves, one connected to the "head space", and the second connected to the dip-tube. A carrier gas is passed down the dip-tube, creating a stream of bubbles containing a gas mixture of trisilane in the carrier gas, which is removed via the head space valve. The concentration of trisilane in that mixture can be controlled by the temperature of the bubbler and the pressure of the carrier gas.

From a regulatory standpoint, Trisilane is not listed on the USEPA's Toxic Substances Control Act ("TSCA") Inventory. It is supplied by Voltaix under a "Low Volume Exemption" (40 CFR 723) and its use is restricted to the formation of silicon and silicon compounds.

A-Si:H films and devices are grown in a multi-chamber PECVD system with a load lock chamber. In such a study, it is important to make sure that the measurement of the  $\text{Si}_3\text{H}_8$  and  $\text{Si}_2\text{H}_6$  gas flows is reliable. For this reason, the  $\text{Si}_3\text{H}_8$  and  $\text{Si}_2\text{H}_6$  gasses, both obtained from Voltaix, Inc., are introduced into the PECVD chamber via a common mass flow controller. The gas factors of the mass flow controller for  $\text{Si}_3\text{H}_8$  and  $\text{Si}_2\text{H}_6$  gasses were calibrated and verified by pressurizing the deposition chamber using  $\text{Si}_3\text{H}_8$  and  $\text{Si}_2\text{H}_6$  gasses separately, both through the same mass flow controller. In addition, the deposition of Si:H films and devices using  $\text{Si}_3\text{H}_8$  and  $\text{Si}_2\text{H}_6$  were carried out alternatively to avoid any unwanted effect due to the systematic and unknown drift, if any, of the deposition equipment and device processing procedures.

While hydrogen dilution is changed during the growth of these films, the other deposition conditions are kept to be the same as the standard 1-layer deposition conditions used for the deposition of high-quality a-Si:H solar cells in the same PECVD system. These conditions: substrate temperature  $T_s$  at 150°C, chamber pressure at 0.6Torr and rf power at 25mW/cm<sup>2</sup>, are kept unchanged for films deposited using both  $\text{Si}_3\text{H}_8$  and  $\text{Si}_2\text{H}_6$ . The hydrogen dilution R was

varied from 71 to 286 and from 75 to 149 using  $\text{Si}_3\text{H}_8$  and  $\text{Si}_2\text{H}_6$  respectively. Various substrates, including quartz, glass (Corning 1737), c-Si wafer, and stainless steel foil, are used for Si:H deposition for various optical, electrical and structural characterization. The film thicknesses range from 250nm to 500nm.

A-Si:H solar cells with n-i-p structure were deposited on Al/ZnO coated stainless steel. Intrinsic-layer deposition condition was the same as described above. The window p-layer was deposited at low  $T_s$ , about 70-100 °C, and high hydrogen dilution. ITO was sputtered on the p-layer as transparent conductive coating. Light soaking was done under white light at 1 sun intensity and the ambient temperature was ~ 40-50C.

Infrared absorption spectroscopy was measured for Si:H films deposited on c-Si substrate in the ranges from  $400\text{cm}^{-1}$  to  $800\text{cm}^{-1}$  and from  $1800\text{cm}^{-1}$  to  $2400\text{cm}^{-1}$  and with a resolution of  $0.33\text{cm}^{-1}$ . The integrated strength for the wagging mode at  $640\text{cm}^{-1}$  was used to obtain the H content (at.%). The stretching modes at  $2000\text{cm}^{-1}$  and  $2100\text{cm}^{-1}$  were used to obtain the microstructure factor  $R^*$  in the film. Gaussian distribution was used to fit the absorption peaks. Transmission spectra were recorded using a Cary 5 spectrophotometer. Scanning range was from 400nm to 2200nm. Thickness was calculated using the method described in the literature.<sup>[1]</sup> Raman scattering was performed to characterize the structure of Si:H films. 488nm laser line from a water-cooled  $\text{Ar}^+$  laser was used for the excitation. Photoconductivity was measured when the samples were annealed in a test chamber purged with  $\text{N}_2$ . A pair of Ag electrodes, ~2 mm apart, were painted on the films. Samples are heated to 180°C and the temperature dependence of dark conductivity is measured during the cooling process, from 180°C to 50°C. Activation energy was measured from a semilog plot ( $\log \sigma$  vs  $1000/T$ ). Photoconductivity was measured using a ELH lamp at  $100\text{ mW/cm}^2$  intensity at room temperature (25°C).

## RESULTS AND DISCUSSIONS

Figure 4-1 shows the deposition rate of intrinsic layers as a function of hydrogen dilution  $R$ . Film thickness was calculated from the transmission spectrum. The deposition rate of  $\text{Si}_3\text{H}_8$  samples is higher than that of  $\text{Si}_2\text{H}_6$  samples when the two films are deposited with the same  $R$ . As  $R$  is increased from 75 to 285 for  $\text{Si}_3\text{H}_8$  samples, deposition rate is decreased from  $0.45\text{ Å/sec}$  to  $0.2\text{ Å/sec}$ . Lower deposition rate is observed for  $\text{Si}_2\text{H}_6$  samples with the same  $R$ . In each series, smaller deposition rate is observed at higher dilution  $R$ . This decrease in deposition rate often accompanies with formation of nanocrystalline phase which is a more ordered structure. The increase in hydrogen dilution provides the required atomic hydrogen to etch out the disordered portion of the growing a-Si:H films and also provide the hydrogen coverage on the growing surface. Thus the deposition rate decreases and simultaneously these factors induce the propagation of nanocrystalline network in the films. It is additionally observed that,  $R_t$ , the hydrogen dilution level at which the transition from amorphous to an amorphous/nanocrystalline silicon mixed phase occurs, is higher for a-Si:H films deposited using  $\text{Si}_3\text{H}_8$ .  $R_t$  is around 200 for  $\text{Si}_3\text{H}_8$  while  $R_t$  is around 150 for  $\text{Si}_2\text{H}_6$ . The deposition rate is also plotted against the atomic dilution ratio,  $R_a = [\text{H}]/[\text{Si}]$ , which is the ratio of number of hydrogen and silicon atoms in the gas. Since  $R_a$  is identical to  $R$  for  $\text{Si}_2\text{H}_6$ , only deposition rate dependence on  $R_a$  for  $\text{Si}_3\text{H}_8$  samples is added in Figure 4-1, as solid triangle symbols. It is further observed that the deposition rate vs  $R_a$  curves are approximately the same for both gasses. Therefore, the deposition rate is more

influenced by the ratio of the total number of Si atoms to hydrogen atoms directed into the chamber rather than the number of Si-containing molecules.

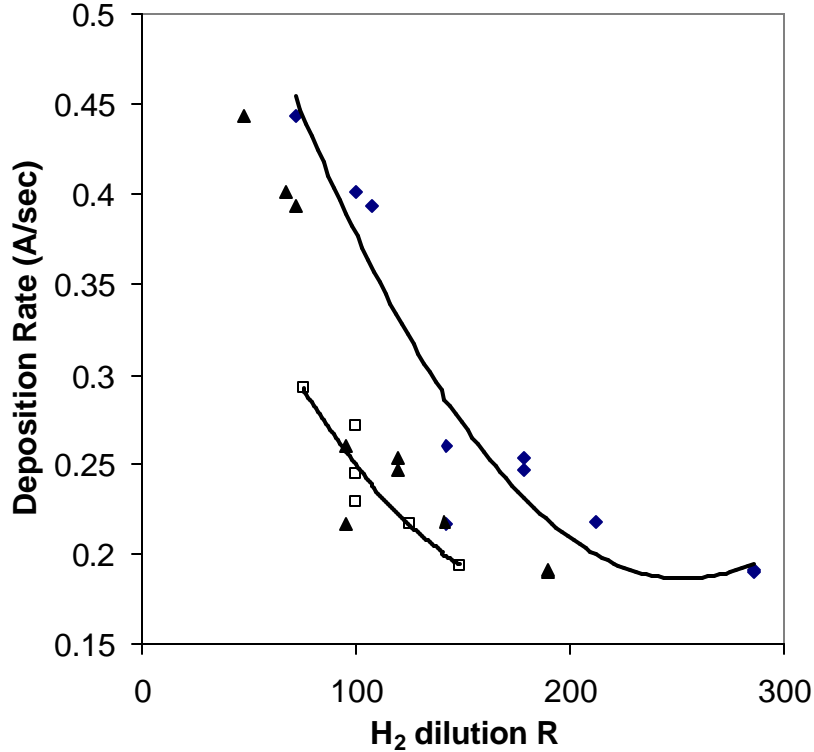


Figure 4-1. Deposition rates of intrinsic a-Si:H film deposited under the conditions of RF power =25mW/cm<sup>2</sup> and T<sub>s</sub>=150°C. Square symbols represent S<sub>2</sub>H<sub>6</sub> series and diamond symbols represent SiH<sub>4</sub> series; The solid triangles represent the relationship between deposition rates and R<sub>a</sub>=[H]/[Si] for SiH<sub>4</sub> series.

It is widely known that high-quality a-Si:H material is often deposited near the transition region from amorphous to nanocrystalline via a hydrogen dilution mediated path. A material deposited near such a transition region is sometimes referred to as protocrystalline or “edge” material. In order to find R<sub>t</sub> for both S<sub>2</sub>H<sub>6</sub> and SiH<sub>4</sub>, a-Si:H films are deposited on a variety of substrates at different R. SiH<sub>4</sub>-deposited films in this study are deposited with R (H<sub>2</sub> (sccm):SiH<sub>4</sub>(sccm)) of: 71 (50:0.7); 107 (75:0.7); 143 (100:0.7); 179 (100:0.56), 213 (100:0.47) and 286 (100:0.35). S<sub>2</sub>H<sub>6</sub>-deposited films in this study are deposited with R (H<sub>2</sub>(sccm):S<sub>2</sub>H<sub>6</sub>(sccm)) of 75 (75:1); 100 (100:1); 125 (100:0.8); and 149 (100:0.67). Figures 2A and 2B show the Raman spectra of two series of films deposited using SiH<sub>4</sub> and S<sub>2</sub>H<sub>6</sub>, respectively. Table 4-1 shows the volume fraction of nc-Si:H phase calculated using approaches described in the literature<sup>[2]</sup>. Figure 4-2A shows that at R=143, the material is still amorphous while at R=179 formation of a-Si:H/nc-Si:H mixed phase starts. The volume fraction of the nc-Si:H phase calculated from the peak intensity is 2.8%. Therefore, R<sub>t</sub> is between 143 and 179 for SiH<sub>4</sub>. For S<sub>2</sub>H<sub>6</sub>-deposited samples, Figure 4-2B indicates that R<sub>t</sub> is between 100 and 125, lower

than that of  $\text{Si}_3\text{H}_8$ . It should be noted that Sample GD1006 with  $R=179$  is thicker than other films such as GD1002. Under a high  $R$ , thicker  $\alpha\text{-Si:H}$  is more likely to have nc-Si:H phase <sup>[3]</sup> It is likely that  $R_t$  for  $\text{Si}_3\text{H}_8$ -deposited films is higher than 179 if the film thickness would be around 170nm (as in GD1002), which is typical for the  $\text{i}$ -layer of  $\alpha\text{-Si:H}$  top component cell in a triple-junction solar cell. As to be described later, solar cells made with  $\text{Si}_3\text{H}_8$  at  $R=179$  showed high  $V_{oc}$ , indicating that  $R_t$  is greater than 179 for  $\text{Si}_3\text{H}_8$ -deposited films with around 170nm thickness. These Raman studies suggest that  $R\sim 100$  and  $R\sim 180$ , for  $\text{Si}_2\text{H}_6$  and  $\text{Si}_3\text{H}_8$ , respectively, may be optimum for deposition of  $\alpha\text{-Si:H}$  solar cell intrinsic layers with thickness around 150 to 200 nm.

The films described in Figure 4-2 and Table 4-1 were also evaluated using Raman with excitation light through the quartz substrates. Such a measurement reveals the structure of the film grown during initial stage of the deposition. Raman scattering measurement show that the  $\alpha\text{-Si:H}$  materials deposited on glass or quartz substrates during the initial stage of deposition is amorphous for all these samples described in Table 4-1 and Fig. 4-2.

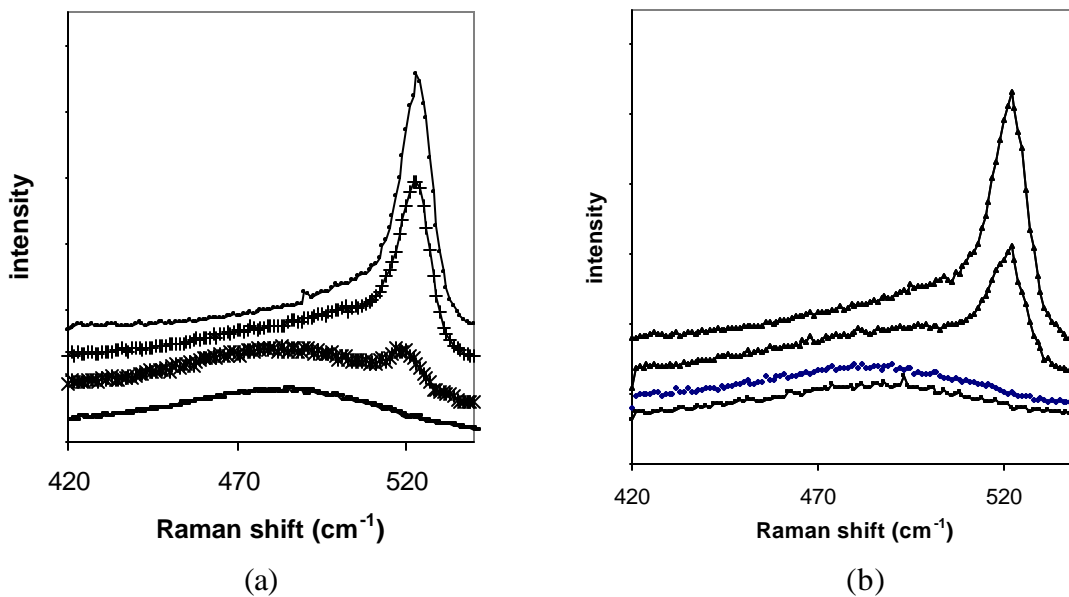


Figure 4-2 Raman spectra of the series of sample deposited using  $\text{Si}_3\text{H}_8$  (2a) and  $\text{Si}_2\text{H}_6$  (2b). In Fig. 4-2a, curves from bottom to top are for  $\text{Si:H}$  deposited with  $R=143, 179, 213$ , and  $286$ . In Fig. 4-2b, curves from bottom to top are for  $\alpha\text{-Si:H}$  deposited with  $R=75; 100; 125$ ; and  $150$ .

Table 4-1. Volume fraction of nanocrystalline silicon phase estimated from Raman spectra for two series of sample. Thicknesses of samples are also included in the Table.

Sample No	Gas precursor	Gas flow (sccm)	Ratio R	Thickness (nm)	nc -Si:H volume frac. (%)
GD1003	Si <sub>2</sub> H <sub>6</sub>	1:75	75	176	N.A.
GD1002	Si <sub>2</sub> H <sub>6</sub>	1:100	100	165	N.A.
GD1004	Si <sub>2</sub> H <sub>6</sub>	0.8:100	125	195	13.6
GD1005	Si <sub>2</sub> H <sub>6</sub>	0.67:100	149	209	37.8
GD1010	Si <sub>3</sub> H <sub>8</sub>	0.7:100	143	234	N.A.
GD1006	Si <sub>3</sub> H <sub>8</sub>	0.56:100	179	340	2.8
GD1009	Si <sub>3</sub> H <sub>8</sub>	0.47:100	213	261	17.7
GD1007	Si <sub>3</sub> H <sub>8</sub>	0.35:100	286	273	57.2

Activation energy  $E_a$  was calculated from temperature dependence of dark conductivity using  $\sigma = \sigma_0 \exp(-E_a/kT)$ . For undoped or n-type a-Si:H,  $E_a$  is approximately the energy difference between the Fermi level and the conduction band edge. Figure 4-3 shows the activation energy as a function of hydrogen dilution R for both Si<sub>3</sub>H<sub>8</sub>- and Si<sub>2</sub>H<sub>6</sub>-deposited samples. For Si<sub>3</sub>H<sub>8</sub>-deposited samples,  $E_a$  is decreased from 0.85 eV at low R to 0.5 eV at high R. This decrease is believed to be due to the narrowing of the bandgaps of the deposited materials when there is a higher volume fraction of nc-Si:H phase in the sample. Similar trend is observed for Si<sub>2</sub>H<sub>6</sub> deposited films. A major difference between the two series of films is that  $E_a$  for Si<sub>2</sub>H<sub>6</sub> samples decreases rapidly when R is increased to 150 while  $E_a$  for Si<sub>3</sub>H<sub>8</sub> samples decreases gradually, over a larger range of R, when R is increased to ~250. The gradual change in  $E_a$  with increasing R may suggest that the range of R for the deposition of a-Si:H/nc-Si:H mixed phase is broader. The exact nature for such a difference between Si<sub>3</sub>H<sub>8</sub> and Si<sub>2</sub>H<sub>6</sub> is unclear.

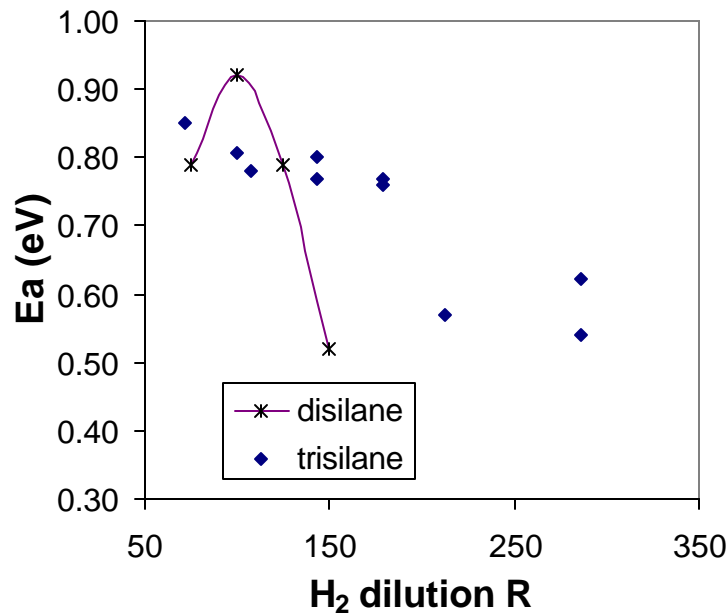


Figure 4.3 Activation energy of a-Si:H films made using  $\text{Si}_2\text{H}_6$  and  $\text{Si}_3\text{H}_8$  as a function of hydrogen dilution R.

Fourier transform infrared spectroscopy (FTIR) was used to measure the content of bonded hydrogen in these Si:H films as well as the amount of hydrogen in different bonding environment. A microstructure factor,  $R^*$ , defined as the fraction of hydrogen in dihydride form among all hydrogen incorporated in the film, is calculated from the integrated strength of the  $2100\text{cm}^{-1}$  peak and  $2000\text{cm}^{-1}$  peak ( $R^* = I(2100\text{ cm}^{-1}) / [I(2100\text{ cm}^{-1}) + I(2000\text{ cm}^{-1})]$ ).<sup>[4]</sup> The microstructure factor  $R^*$  is plotted against dilution R for  $\text{Si}_3\text{H}_8$  and  $\text{Si}_2\text{H}_6$  deposited films in Fig. 4-4.

Figure 4-4 shows that for both series of films,  $R^*$  decreases initially and increases again at higher R. The initial decrease is associated with the reduction of undesirable micro-voids in the films. The increase in  $R^*$  at higher dilution R is believed to be associated with the nc-Si:H formation—hydrogen at grain boundaries bonds to Si mostly in dihydride form. In addition to these general trends, there are noticeable difference in the  $R^*$  vs R between the two series of films. The increase in  $R^*$  occurs at a higher R for  $\text{Si}_3\text{H}_8$ -deposited films, indicating that  $R^*$  is higher for  $\text{Si}_3\text{H}_8$ . It is interesting to notice that for films deposited without hydrogen dilution ( $R=0$ ),  $R^*$  is lower for  $\text{Si}_3\text{H}_8$  films. This is unexpected because the atomic ratio of H to Si is lower in  $\text{Si}_3\text{H}_8$  than  $\text{Si}_2\text{H}_6$ . The lower  $R^*$  (at  $R=0$ ) for  $\text{Si}_3\text{H}_8$  suggests that  $\text{Si}_3\text{H}_8$  is dissociated in plasma into a form that is more desirable for the formation of dense a-Si:H. However, one needs to be cautious in drawing a general conclusion based on these results since other deposition conditions such as rf power, chamber pressure, substrate temperature may impact  $R^*$  at  $R=0$ .

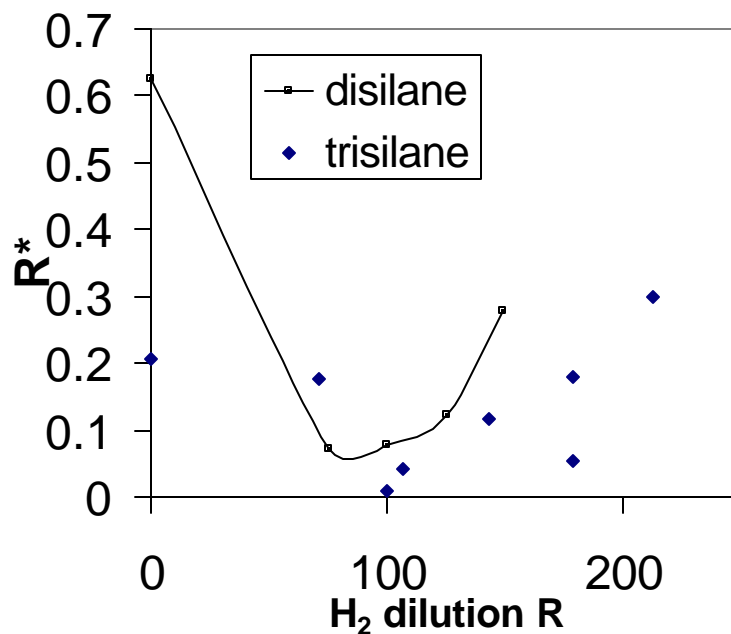


Figure 4-4 Microstructure factor  $R^*$  as a function of hydrogen dilution  $R$ .

Bonded hydrogen content in the Si:H films is estimated from the integrated peak strength of the Si-H wagging mode ( $640\text{ cm}^{-1}$ ). Figure 4-5 shows the H content in the a-Si:H films for both series. For  $\text{Si}_2\text{H}_6$  samples, H content is approximately 15-20 at.% at  $R \sim 100$ . For  $\text{Si}_3\text{H}_8$  samples, H content is approximately 20% at  $R \sim 150$ , and decreases down to 6% at  $R > 250$ . The absolute value of H content depends on the calibration factor used and the values in Figure 4-5 may not be accurate in the absolute scale. However, relative change in H content is believed to be reproducible.



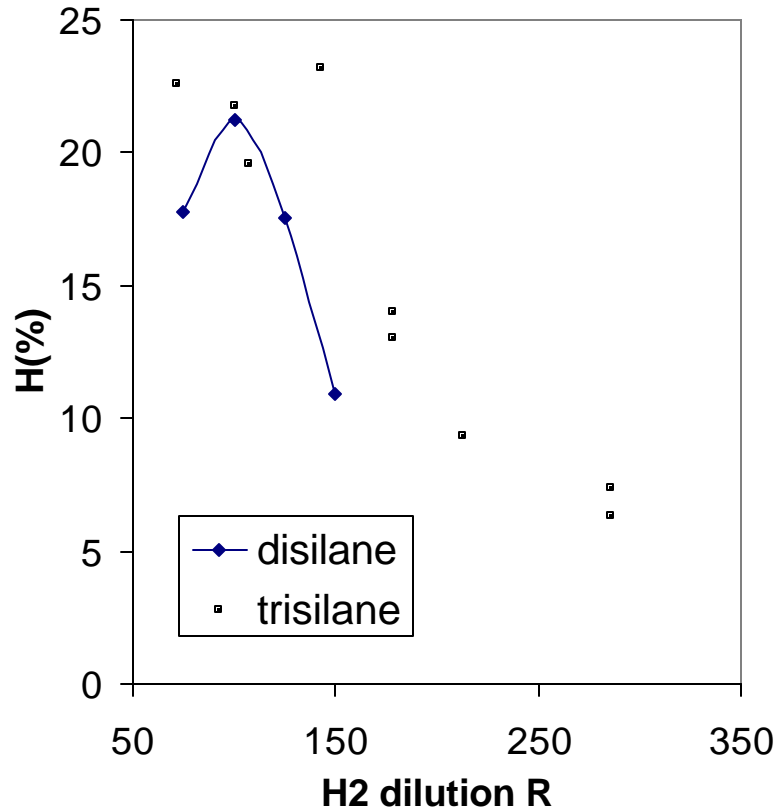


Figure 4-5. H content estimated from FTIR spectra as a function of H<sub>2</sub> dilution R

Figure 4-6 shows photosensitivity of these a-Si:H films, which is the ratio of photoconductivity under 1 sun illumination and the dark-conductivity. The photosensitivity decreases with increased volume fraction of nc-Si:H phase due to the defects near the grain boundaries. The highest photosensitivity,  $1 \times 10^6$ , occurs at  $R \sim 100$ , or  $R_t$ , for  $\text{Si}_2\text{H}_6$  samples. The photosensitivity then decreases with increasing R, indicating the increase of nanocrystalline fraction in the material. The highest photosensitivity is nearly the same for the two series of samples. However, the decrease in photosensitivity at  $R > R_t$  is more gradual for  $\text{Si}_3\text{H}_8$ , similar to the gradual decrease in its activation energy.

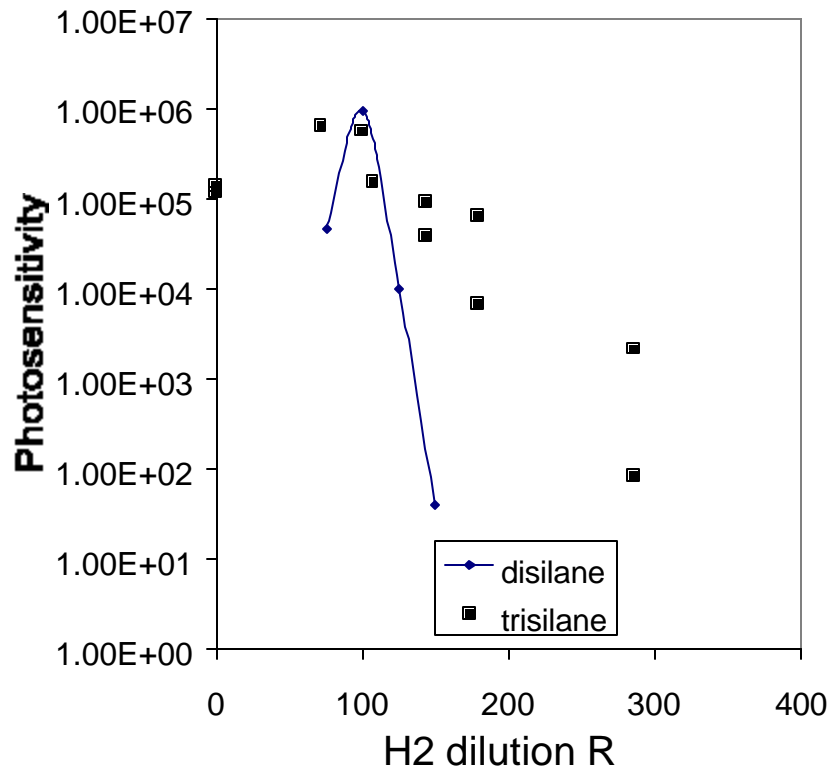


Figure 4-6. Photosensitivity of a-Si:H films deposited using  $\text{Si}_2\text{H}_6$  and  $\text{Si}_3\text{H}_8$  as a function of hydrogen dilution.

Results in Figures 3-6 indicate that when  $\text{Si}_3\text{H}_8$  is used for the deposition of Si, the transition from amorphous to nanocrystalline is more gradual as compared with that for  $\text{Si}_2\text{H}_6$ . In other words, the H dilution range for mixed phase is broader when  $\text{Si}_3\text{H}_8$  is used. Material with optimal optoelectronic performance is grown with  $R \sim 180$  at  $T_s \sim 150$  oC when  $\text{Si}_3\text{H}_8$  is used. These materials have similar properties to those materials deposited using  $\text{Si}_2\text{H}_6$  with  $R \sim 100$ .

In order to further verify the findings from this materials study, two series of solar cells were fabricated using  $\text{Si}_3\text{H}_8$  and  $\text{Si}_2\text{H}_6$  with different hydrogen dilution  $R$  for the  $i$ -layers. When all other device parameters are kept the same,  $V_{oc}$  of the solar cells are directly related to the  $i$ -layer bandgap. When appropriate level of  $R$  is used and the Si:H is near the transition from amorphous to mixed phase,  $V_{oc}$  is the highest. At higher  $R$ ,  $V_{oc}$  drops due to the formation of nc-Si:H in the  $i$ -layer. Figure 4-7 shows the  $V_{oc}$  of solar cells as a function of  $R$  for  $i$ -layers made using  $\text{Si}_3\text{H}_8$  and  $\text{Si}_2\text{H}_6$  at different  $R$ . For  $\text{Si}_2\text{H}_6$  devices,  $V_{oc}$  reaches its highest value (1.014V) at  $R \sim 100$ , while for  $\text{Si}_3\text{H}_8$  devices,  $V_{oc}$  reaches its highest value (1.010V) at  $R \sim 180$ . These results on solar cell devices are consistent with the findings in the materials study of single-layer films deposited on glass. Both series of solar cells, with  $\sim 200\text{nm}$  thick  $i$ -layers, were illuminated with white light at 1 sun intensity. After 100 hours of light soaking,  $\text{Si}_3\text{H}_8$  devices degraded 11.7% and  $\text{Si}_2\text{H}_6$  devices degraded 13.2%. These degradations are considered to be the same within experimental variations.

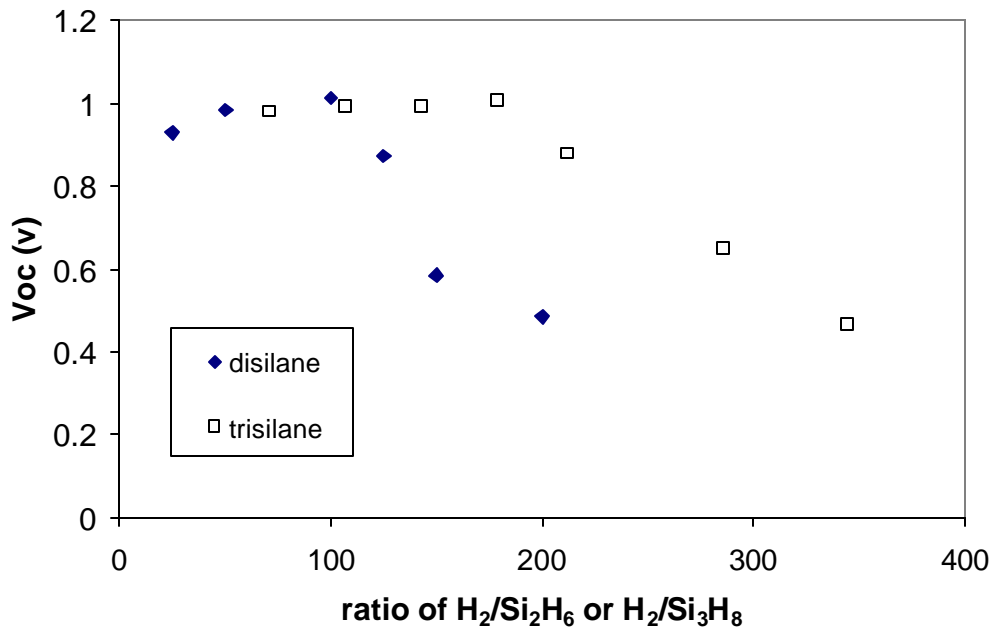


Figure 4-7 Open circuit voltage versus  $H_2$  dilution for  $Si_2H_6$  and  $Si_3H_8$  devices.

## SUMMARY

$Si:H$  films and solar cells deposited using  $Si_3H_8$  and using  $Si_2H_6$  are compared. At the same hydrogen dilution,  $Si_3H_8$  leads to higher deposition rate. However, at the same atomic ratio of hydrogen and silicon, the deposition rate of  $Si:H$  using  $Si_3H_8$  and  $Si_2H_6$  is approximately the same. The deposition rate is more influenced by the ratio of the total number of Si atoms to hydrogen atoms introduced into the chamber rather than the number of Si-containing molecules. Measurement of activation energy, microstructure and photosensitivity indicate that 1) the transition from amorphous to amorphous/nanocrystalline mixed phase occurs at a higher hydrogen dilution level when  $Si_3H_8$  is used; and 2) the transition from amorphous to mixed phase is more gradual for  $Si_3H_8$  as compared with  $Si_2H_6$ . When appropriate level of R is used and the a- $Si:H$  is near the transition from amorphous to mixed phase,  $V_{oc}$  is the highest. At higher R,  $V_{oc}$  decreases due to the formation of nc- $Si:H$  in the i-layer. For  $Si_2H_6$  devices,  $V_{oc}$  reaches its highest value (1.014V) at  $R \sim 100$ , while for  $Si_3H_8$  devices,  $V_{oc}$  reaches its highest value (1.010V) at  $R \sim 180$ . These results on solar cell devices are consistent with the findings in the materials study of single-layer films deposited on glass.

## References

1. R. Swanepoel, J physics.E Sci.instrum. Vol 16,1983 p1914-1922.
2. H. Shanks etc. Phys. Stat. Sol (B) 100,43 (1980).
3. A. Ferlauto, R. Koval, C. Wronski, R. Collins, *Appl. Phys. Lett.* **80**, 2666 (2002).
4. M. H. Brodsky, M. Cardona, J. J. Cuomo, *Phy. Rev. B* 16 (1977) 3556.

## Section 5 Deposition of a-SiGe:H and nc-SiGe:H films using HWCVD

Contributors: Xinmin Cao, Henry S. Povolny and Xunming Deng

### Abstract

Using hot-wire chemical vapor deposition (HWCVD) with coil-shaped tungsten filament, amorphous and nanocrystalline silicon-germanium (SiGe) films are deposited with a filament temperature  $T_{\text{fil}}$  in the range of 1700 – 2000 °C, a substrate temperature  $T_{\text{sub}}$  in the range of 150 – 400 °C, and a gas mixture with a disilane/germane/hydrogen gas mixture ratio of 3.4/1.7/7, 2.4/1.7/7 and 0/1.7/7, respectively. The structural properties of as-deposited films are investigated by Scanning electron microscopy (SEM), X-ray diffraction (XRD), Raman scattering and Fourier transform infrared (FTIR) absorption spectroscopy. The influence of the filament length on film property is also studied.

### Introduction

Amorphous SiGe alloys are used as i-layers in the tandem and triple-junction amorphous silicon based solar cells. By varying the amount of Ge in the i-layer, the band gap can be varied from ~1.1 eV (in pure a-Ge:H films) to 1.8 eV (pure a-Si:H) films. Using a triple cell structure and with a PECVD method, United Solar Systems Corp. fabricated a-Si/a-SiGe/a-SiGe solar cells with 13% stabilized efficiency <sup>[1]</sup>. Using an intrinsic a-SiGe:H absorber layer deposited by HWCVD method, Lill et al achieved solar cells with an  $\eta_{\text{initial}} = 6.4\%$  for pin cell structure <sup>[2]</sup> and Wang et al achieved solar cells with  $\eta_{\text{initial}} = 7.3\%$  for nip cell structure <sup>[3]</sup>, respectively.

Recently nc-Si:H material related investigation has attracted a great deal of attention for solar cell application. Schropp et al yielded  $\eta = 5.97\%$  for HWCVD nip solar cells with a nanocrystalline absorber i-layer of an amorphous / nanocrystalline phase transition <sup>[4]</sup>. By integrating nc-Si:H absorber i-layers deposited by HWCVD, Klein et al achieved solar cells with an  $\eta_{\text{initial}} = 7.4\%$  for pin cell structure and  $\eta_{\text{initial}} = 9.4\%$  for nip cell structure, respectively <sup>[5]</sup>. It was assumed, by deposition near the amorphous to nanocrystalline phase transition, a highly conductive nc-Si:H with a compact morphology and effective grain boundary passivation could be achieved and thus the defect density in the films could be greatly reduced.

At the University of Toledo, we deposited a-SiGe:H and nc-SiGe:H films by HWCVD with different deposition parameters. The structural properties of as-deposited films are investigated by Scanning electron microscopy (SEM), X-ray diffraction (XRD), Raman scattering and Fourier transform infrared (FTIR) absorption spectroscopy. Our goal is to find suitable HW deposition conditions for SiGe films containing amorphous / nanocrystalline phase transition and thus to obtain high quality nc-SiGe:H films with a relatively high deposition rate for solar cell applications.

## Experimental

The SiGe films, approximately up to 1.3  $\mu\text{m}$  thick, are deposited on 7059 glass, crystalline silicon (c-Si) wafer and stainless steel (SS) substrates using Hot-Wire Chemical Vapor Deposition (HWCVD) with a coil-shaped tungsten filament in an ultrahigh-vacuum, multi-chamber, load-locked deposition system. The HWCVD system consists of a high vacuum chamber, a substrate holder, a coiled filament perpendicular to the substrate, two annular gas inlets near the substrate and one axial gas inlet directed through the filament coil, a gas confinement cup and an annular RF electrode for PECVD. The substrate holder, capable of holding a 10 cm by 10 cm substrate, is inverted over the gas confinement cup. Detailed description of this HWCVD system can be seen elsewhere <sup>[6, 7]</sup>.

Two types (Type L and Type S) of coil-shaped filament with the same filament diameter of 0.75 mm but with different filament lengths have been used in this study. The parameters of these two types of filament coils are shown in Table 5-1. The coil-shaped filament Type L is made of tungsten wire 100 cm long and of 0.75 mm diameter, wound in a coil of approximately 7 mm in diameter and 47 mm long with around 45 turns. On the other hand, for the coil-shaped filament Type S we used only 30 cm long same tungsten wire, wound in a coil of approximately 8 mm in diameter and 20 mm in length with around 10 turns. The tops of the filament Type L and Type S both have the same distance of about 6 cm from the substrate.

*Table 5-1: The parameters of the coil-shaped filament used in this study*

Filament: tungsten (W), diameter of 0.75 mm, coil shaped				
Type	Filament length	Coil turns	Coil length	Coil diameter
Type L	100 cm	45	47 mm	7 mm
Type S	30 cm	10	20 mm	8 mm

A gas mixture with a disilane/germane/hydrogen gas mixture ratio of 3.4/1.7/7, 2.4/1.7/7 and 0/1.7/7 is used for depositing amorphous and nanocrystalline silicon-germanium (SiGe) films. The filament temperature  $T_{\text{fil}}$  is set in the range of 1700 – 2000  $^{\circ}\text{C}$ , while the substrate temperature  $T_{\text{sub}}$  in the range of 150 – 400  $^{\circ}\text{C}$ .

Transmission measurements in the Vis-NIR range (400 nm – 3300 nm) are carried out to determine the thickness, optical gap and refractive index of these films.

The film surface topographies are investigated by Scanning electron microscopy (SEM); the crystalline fraction of the films are obtained from Raman scattering spectroscopy; the orientation and size of crystallites are detected by X-ray diffraction (XRD); and the bonded hydrogen content in the films and its bonding nature with Si and Ge is determined from Fourier transform infrared (FTIR) absorption spectroscopy.

## Results and Discussions

### 3.1 Dependence of Deposition rate and surface topography on $T_{\text{fil}}$ and $T_{\text{sub}}$

The deposition rate  $r_{\text{dep}}$  of SiGe-films deposited by HWCVD is significantly influenced by the filament temperature  $T_{\text{fil}}$ , but not that much by the substrate temperature  $T_{\text{sub}}$ , as shown in Figure 5-1. At a  $\text{Si}_2\text{H}_6$  flow rate  $F_{\text{Si}_2\text{H}_6} = 3.4$  sccm,  $\text{GeH}_4$  flow rate  $F_{\text{GeH}_4} = 1.7$  sccm,  $\text{H}_2$  flow rate  $F_{\text{H}_2} = 7.0$  sccm, a total process pressure  $p = 3.1$  mTorr and a substrate temperature  $T_{\text{sub}} = 200^\circ\text{C}$ , the deposition rate  $r_{\text{dep}}$  increases from  $2.8 \text{ \AA/s}$  to  $7.9 \text{ \AA/s}$  with increasing filament temperature  $T_{\text{fil}}$  from  $1800^\circ\text{C}$  to  $2000^\circ\text{C}$ . While the substrate temperature is at  $T_{\text{sub}} = 300^\circ\text{C}$ , the deposition rate  $r_{\text{dep}}$  increases from  $3.3 \text{ \AA/s}$  to  $8.7 \text{ \AA/s}$  with increasing filament temperature  $T_{\text{fil}}$  from  $1800^\circ\text{C}$  to  $2000^\circ\text{C}$ . All the four depositions have the same deposition time of  $t = 15$  min. The increase in deposition rate at the higher  $T_{\text{fil}}$  may be attributed to the higher gas cracking efficiency due to higher filament temperature where availability of growth precursors ( $\text{SiH}_3$  etc) and atomic hydrogen (H) both are expected to be high enough. In the further structural characterizations we shall verify the effects of these factors on material properties.

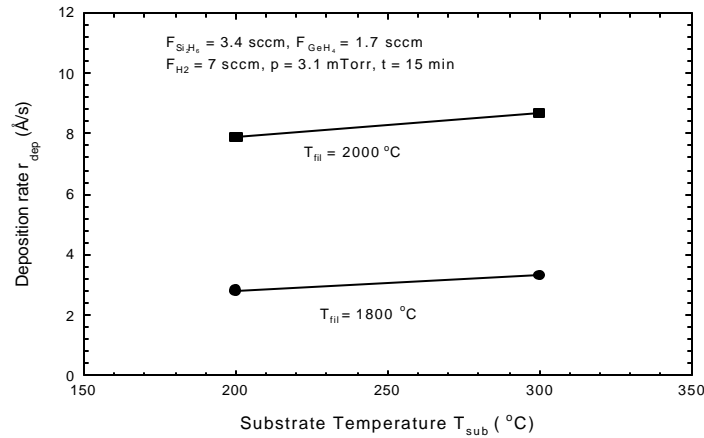


Fig. 5-1. Dependence of the deposition rate  $r_{\text{dep}}$  on the filament temperature  $T_{\text{fil}}$  and the substrate Temperature  $T_{\text{sub}}$  at a  $\text{Si}_2\text{H}_6$  flow rate  $F_{\text{Si}_2\text{H}_6} = 3.4$  sccm,  $\text{GeH}_4$  flow rate  $F_{\text{GeH}_4} = 1.7$  sccm,  $\text{H}_2$  flow rate  $F_{\text{H}_2} = 7.0$  sccm, a total process pressure  $p = 3.1$  mtorr.

The film topographical structures of the above four SiGe samples are also characterized by SEM. Figure 5-2a and 2b show the SEM images of the two samples deposited at  $T_{\text{fil}} = 1800^\circ\text{C}$  with the substrate temperature of  $T_{\text{sub}} = 200^\circ\text{C}$  and  $T_{\text{sub}} = 300^\circ\text{C}$ , respectively. The two films have relatively smooth surface. Figure 5-2c and 2d show the SEM images of the two samples deposited at  $T_{\text{fil}} = 2000^\circ\text{C}$  with the substrate temperature of  $T_{\text{sub}} = 200^\circ\text{C}$  and  $T_{\text{sub}} = 300^\circ\text{C}$ , respectively. These films at  $T_{\text{fil}} = 2000^\circ\text{C}$  have very rough surfaces. This may be results from the production of nanocrystalline SiGe grains at a relative high deposition rate.

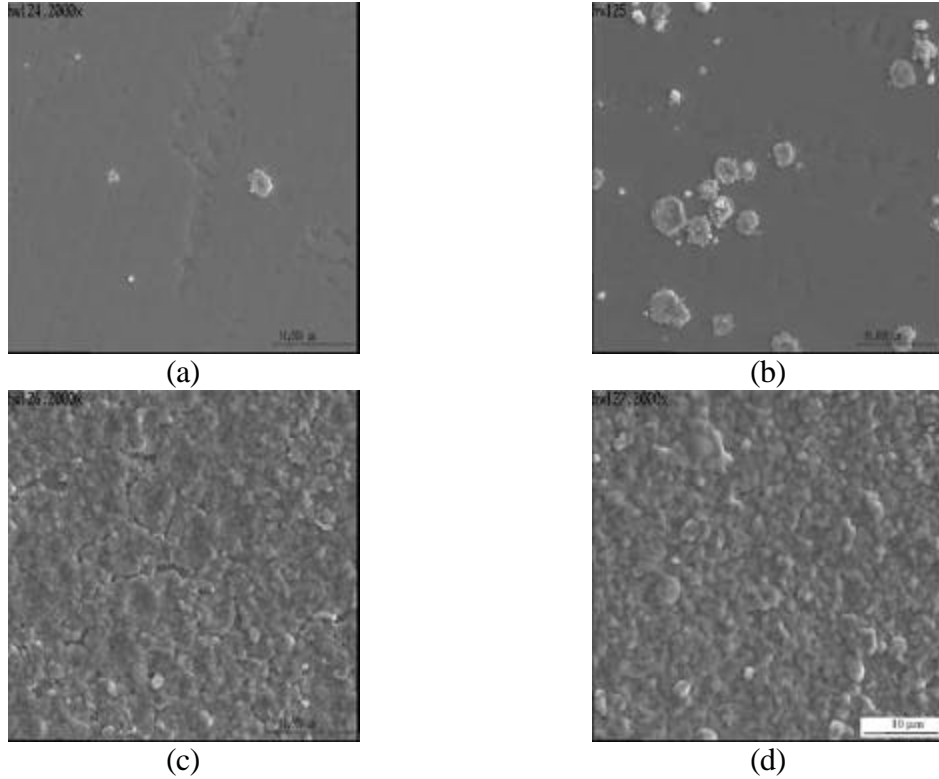


Fig. 5-2. Top-view SEM images of SiGe samples deposited at a  $\text{Si}_2\text{H}_6$  flow rate  $F_{\text{Si}_2\text{H}_6} = 3.4$  sccm,  $\text{GeH}_4$  flow rate  $F_{\text{GeH}_4} = 1.7$  sccm,  $\text{H}_2$  flow rate  $F_{\text{H}_2} = 7.0$  sccm, a total process pressure  $p = 3.1$  mtorr using a)  $T_{\text{fil}} = 1800^\circ\text{C}$  and  $T_{\text{sub}} = 200^\circ\text{C}$ , b)  $T_{\text{fil}} = 1800^\circ\text{C}$  and  $T_{\text{sub}} = 300^\circ\text{C}$ , c)  $T_{\text{fil}} = 2000^\circ\text{C}$  and  $T_{\text{sub}} = 200^\circ\text{C}$ , and d)  $T_{\text{fil}} = 2000^\circ\text{C}$  and  $T_{\text{sub}} = 300^\circ\text{C}$ .

### 3.2 Dependence of film crystallinity on different $T_{\text{fil}}$ , $T_{\text{sub}}$ and gas mixtures

Raman measurements are done on a series of SiGe films, which are deposited with different  $\text{GeH}_4$ ,  $\text{Si}_2\text{H}_6$  and  $\text{H}_2$  gas mixtures at a filament temperature  $T_{\text{fil}}$  ranged from  $1800^\circ\text{C}$  to  $2000^\circ\text{C}$  and a substrate temperature  $T_{\text{sub}}$  ranged from  $150$  to  $300^\circ\text{C}$ . From the Raman spectra as shown in Fig. 5-3, the Raman characteristic vibrations of dominant nanocrystalline phases could be observed clearly. Crystalline Si-Si TO band near  $500\text{ cm}^{-1}$ , crystalline Si-Ge TO band near  $400\text{ cm}^{-1}$  and crystalline Ge-Ge TO band near  $300\text{ cm}^{-1}$  appear in the Raman spectra. It can be seen that the positions and intensities of the Si-Si, Si-Ge and Ge-Ge Raman peaks are obviously shifted and changed with the disilane/germane/hydrogen gas mixture ratio  $R$ . The Raman spectra of the HW samples HW124, HW125, HW126, HW127 and HW132, which are deposited at a disilane/germane/hydrogen gas mixture ratio of  $3.4/1.7/7$  corresponding to  $R_{\text{H}} (= [\text{H}_2]/([\text{Si}_2\text{H}_6] + [\text{GeH}_4] + [\text{H}_2]))$  of  $58\%$  have a Si-Si Raman peak centered at  $507\text{ cm}^{-1}$ , Si-Ge Raman peak at  $400\text{ cm}^{-1}$  and Ge-Ge Raman peak at  $282\text{ cm}^{-1}$ . The intensity of the Si-Si Raman peak is also higher than those of Ge-Si and Ge-Ge Raman peaks. The Si-Si TO band in the nanocrystalline SiGe films are centered around  $507\text{ cm}^{-1}$  and have a peak shift of about  $13\text{ cm}^{-1}$  as compared to the crystalline Si-Si TO band centered near  $520\text{ cm}^{-1}$  in the single crystalline Si

films. This suggests that with the presence of Ge in the SiGe film the crystalline Si-Si bonding length becomes a little bigger than normal.

The Raman intensity of Ge-Ge and Si-Ge peak increases with increasing germane content in the gas mixture, meanwhile the Raman peaks are also shifted. As shown in the Raman spectra of the samples HW128, HW129, HW130 and HW131 with a disilane/germane/hydrogen gas mixture ratio of 2.4/1.7/7 corresponding to  $R_H$  of 63 %, Si-Si peak is shifted to  $502 \text{ cm}^{-1}$ , Si-Ge Raman peak to  $404 \text{ cm}^{-1}$  and Ge-Ge Raman peak to  $287 \text{ cm}^{-1}$ , while the intensity of Si-Ge and Ge-Ge peak also increase.

Raman measurements are also done on pure Ge films of the HW samples HW133-136 deposited with a disilane/germane/hydrogen gas mixture ratio of 0/1.7/7 (without disilane) corresponding to  $R_H$  of 80%, and only sharp Ge-Ge TO peaks centered near  $300 \text{ cm}^{-1}$  are present in these Raman spectra.

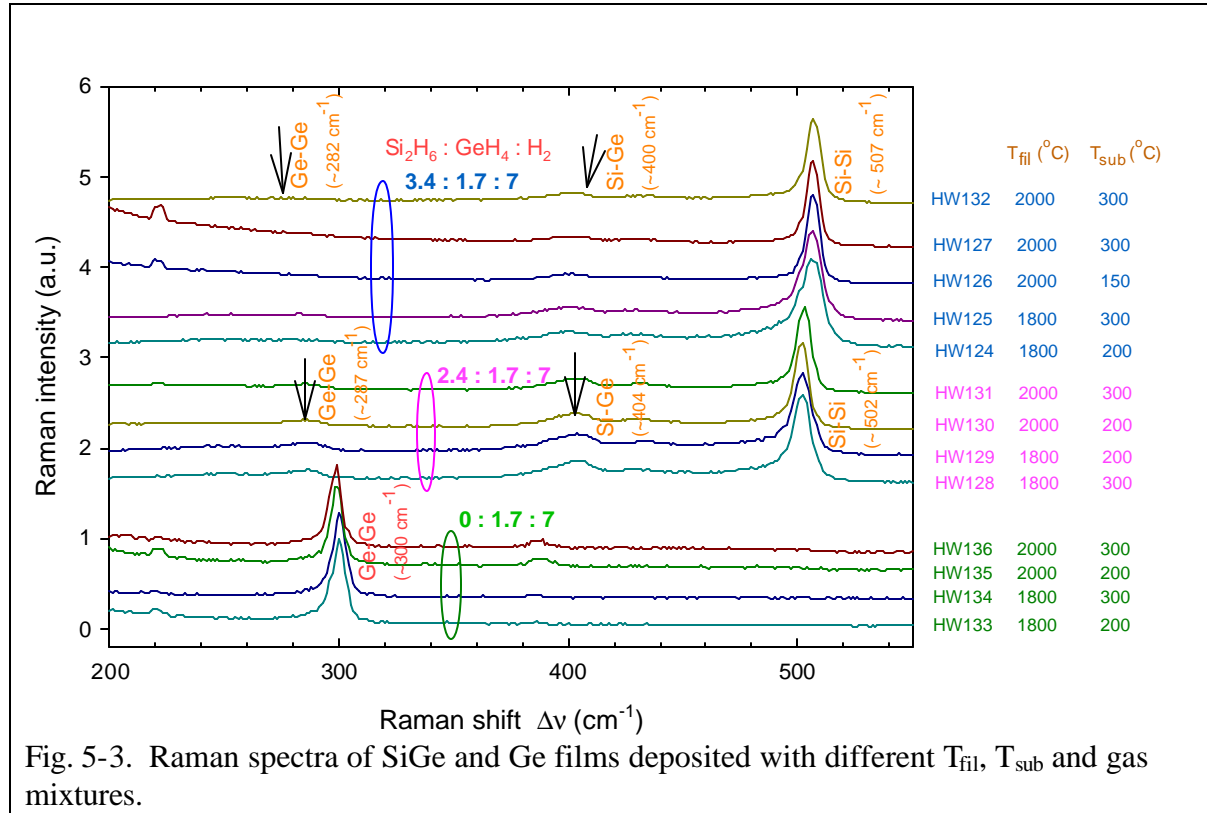


Fig. 5-3. Raman spectra of SiGe and Ge films deposited with different  $T_{\text{fil}}$ ,  $T_{\text{sub}}$  and gas mixtures.

The filament temperature  $T_{\text{fil}}$  and substrate temperature  $T_{\text{sub}}$  have influences on the film growth of amorphous and nanocrystalline phases. The Raman spectrum of sample HW127 deposited at  $T_{\text{fil}} = 2000$  and  $T_{\text{sub}} = 300 ^{\circ}\text{C}$  has a narrow Si-Si TO band centered at  $507 \text{ cm}^{-1}$  with a FWHM of only  $7 \text{ cm}^{-1}$ , which indicates HW127 is nanocrystalline SiGe with nearly 79% volume fraction of nc-SiGe phase. With decreasing filament temperature  $T_{\text{fil}}$  and substrate temperature  $T_{\text{sub}}$ , as shown in the Raman spectrum of sample HW124 deposited at  $T_{\text{fil}} = 1800$  and  $T_{\text{sub}} = 200 ^{\circ}\text{C}$ , the Si-Si band width FWHM increases to  $14 \text{ cm}^{-1}$ , meanwhile the left-side shoulder of Si-Si TO band rises. This indicates that HW124 is characteristic of nanocrystalline



SiGe with mixed-phase contributions of aSiGe:H and nc-SiGe, and the crystalline volume fraction is  $X_c \sim 60\%$ .

Figure 5-4 shows the grazing incidence diffraction (GID) X-ray pattern of the SiGe film deposited on a quartz glass substrate at a  $\text{Si}_2\text{H}_6$  flow rate of  $F_{\text{Si}_2\text{H}_6} = 3.4$  sccm,  $\text{GeH}_4$  flow rate of  $F_{\text{GeH}_4} = 1.7$  sccm,  $\text{H}_2$  flow rate of  $F_{\text{H}_2} = 7.0$  sccm, a total process pressure of  $p = 2.5$  mTorr, a substrate temperature of  $T_{\text{sub}} = 200$  °C and a filament temperature  $T_{\text{fil}} = 1800$ °C for 10 min with a film thickness of  $d = 141$  nm. In the GID X-ray spectrum, diffraction at the SiGe planes (111) centered at  $2\theta = 28.30^\circ$ , (220) centered at  $2\theta = 46.96^\circ$  and (311) centered at  $2\theta = 55.66^\circ$  can be seen clearly. With comparing the relative peak heights of (220) and (311) peaks to (111) peak, it can be determined that the crystallites of this SiGe film are randomly distributed. With X-ray diffraction patterns the crystallite size  $d_{x\text{-ray}}$  can be calculated from the Debye-Scherrer equation.<sup>[8]</sup> The crystallite size of this SiGe film calculated from the peak (111) is  $d_{x\text{-ray}} = 17$  nm.

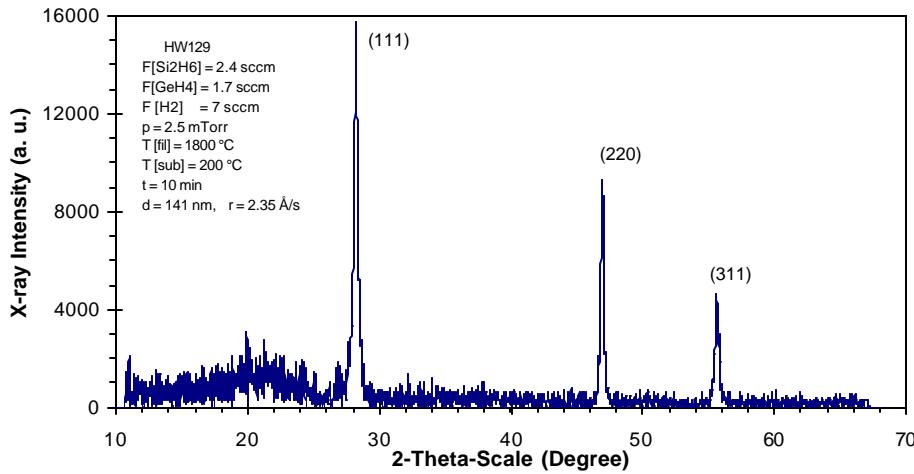
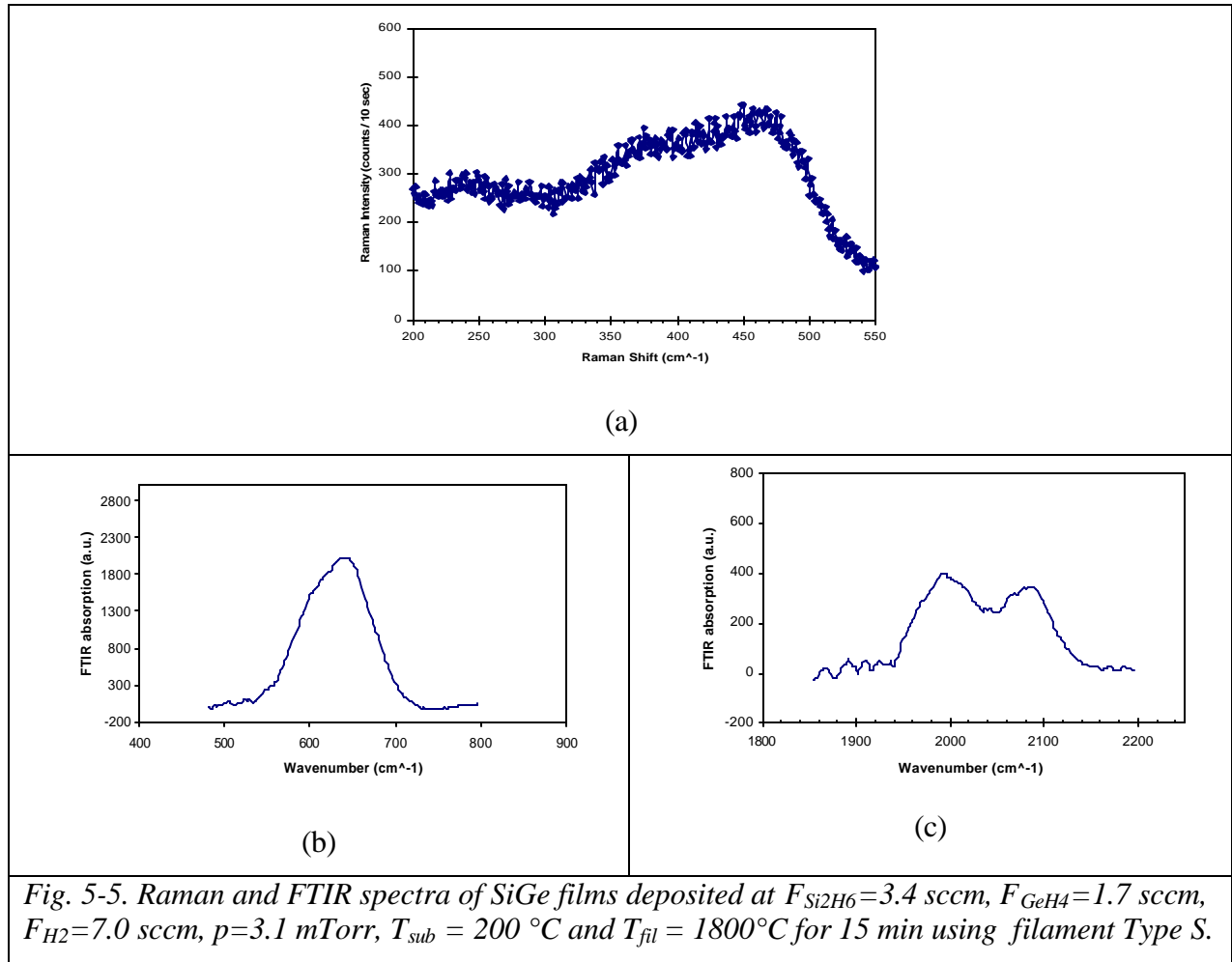


Fig. 5-4. The GID X-ray spectrum of the SiGe film deposited at  $F_{\text{Si}_2\text{H}_6} = 3.4$  sccm,  $F_{\text{GeH}_4} = 1.7$  sccm,  $F_{\text{H}_2} = 7.0$  sccm,  $p = 2.5$  mTorr,  $T_{\text{sub}} = 200$  °C and  $T_{\text{fil}} = 1800$ °C for 10 min with a film thickness of  $d = 141$  nm.

### Influence of filament length

The above described SiGe and Ge films all have been deposited using the coil-shaped filament Type L with a typically filament length of 100cm. The Raman results show that all these films are of dominant nanocrystalline phases with the crystalline volume fraction  $X_c > 80\%$  even though the filament temperature is  $T_{\text{fil}} \sim 1800$  °C and the substrate temperature as low as  $T_{\text{sub}} \sim 150$  °C. The hydrogen content and bonding structure is determined from Fourier transform infrared (FTIR) absorption spectroscopy. The FTIR results show that the hot-wire nc-SiGe films have very small hydrogen contents of  $< 2\%$ , which are nearly undetectable by our FTIR system.

If the filament is replaced with the coil-shaped filament Type S with a typically filament length of 30 cm, the film structures and deposition rates are greatly changed although the other deposition parameters are maintained at same values. Using filament Type S instead of Type L, one set of four deposition runs is made at  $F_{\text{Si}_2\text{H}_6} = 3.4$  sccm,  $F_{\text{GeH}_4} = 1.7$  sccm,  $F_{\text{H}_2} = 7.0$  sccm,  $t = 15$  min and  $p = 3.1$  mTorr by setting  $T_{\text{sub}} = 200$  °C and 300 °C,  $T_{\text{fil}} = 1800$ °C and 2000°C, respectively. The four depositions have a nearly same deposition rate of about 5.7 Å/s. Raman results show that the four samples are characteristic of nearly 100% amorphous SiGe phase. As shown in Fig. 5-5a, the Raman spectrum of a-SiGe layer deposited at  $T_{\text{sub}} = 200$  °C and  $T_{\text{fil}} = 1800$ °C consists of three main broad bands which are due to TO-mode Si-Si ( $\sim 465$   $\text{cm}^{-1}$ ), Si-Ge ( $\sim 370$   $\text{cm}^{-1}$ ) and Ge-Ge ( $\sim 250$   $\text{cm}^{-1}$ ) vibrations.



*Fig. 5-5. Raman and FTIR spectra of SiGe films deposited at  $F_{\text{Si}_2\text{H}_6} = 3.4$  sccm,  $F_{\text{GeH}_4} = 1.7$  sccm,  $F_{\text{H}_2} = 7.0$  sccm,  $p = 3.1$  mTorr,  $T_{\text{sub}} = 200$  °C and  $T_{\text{fil}} = 1800$ °C for 15 min using filament Type S.*

Figure 5-5b and Figure 5-5c shows the FTIR absorption spectrum of this sample in the region of 400 – 800  $\text{cm}^{-1}$  and 1800 – 2200  $\text{cm}^{-1}$ , respectively. The FTIR spectrum in 400 – 800  $\text{cm}^{-1}$  region has a peak centered at 640  $\text{cm}^{-1}$  and a shoulder at 590  $\text{cm}^{-1}$  corresponding to Si-H and Ge-H wagging modes respectively. A hydrogen content of about 7.6% is found out in this SiGe film by calculating the area under this curve in 400 – 800  $\text{cm}^{-1}$  region. The FTIR spectrum in 1800 – 2200  $\text{cm}^{-1}$  region has a peak centered at 1992  $\text{cm}^{-1}$  and a peak at 2086  $\text{cm}^{-1}$  corresponding

to Si-H and Si-H<sub>2</sub> stretching modes respectively. A Si-H<sub>2</sub>/[Si-H+ Si-H<sub>2</sub>] ratio of 0.43 are determined in this film by calculating the area under the corresponding peaks in 1800 – 2200 cm<sup>-1</sup> region.

From the Raman and FTIR results, it can be suggested that using the Filament Type L of 100 cm long, the disilane/germane/hydrogen gas mixture of 3.4/1.7/7, 2.4/1.7/7 and 0/1.7/7 corresponding to R<sub>H</sub> of 58% - 80%, has a high gas cracking efficiency resulting in the reaction area over the substrate with a high density of reactive hydrogen atoms, thus nanocrystalline SiGe films with high crystalline fractions of > 80% but with low hydrogen contents of < 2% are preferably grown. While the Filament Type S with a length of 30 cm has a relative lower gas cracking effect, as a result, only amorphous SiGe are preferably produced with the disilane/germane/hydrogen gas mixture ratio of 3.4/1.7/7.

#### 4. Summary

Nanocrystalline SiGe films deposited at a rate about 8 Å/s result in rough surfaces. The Raman spectrum of nanocrystalline SiGe films consist of three main peaks which are due to TO-mode Si-Si (~500 cm<sup>-1</sup>), Si-Ge (~400 cm<sup>-1</sup>), Ge-Ge (~300 cm<sup>-1</sup>). Peak positions and intensities are sensitive to Si/Ge content in layers, which related to gas flow ratio of Si<sub>2</sub>H<sub>6</sub>/GeH<sub>4</sub>/H<sub>2</sub>. Using a filament of 100 cm long, nanocrystalline SiGe films with crystalline fractions of > 80% and low hydrogen contents of < 2% are preferably grown. Using a short filament with length of 30cm, deposition of amorphous rather than nanocrystalline materials is obtained. The Raman spectrum of amorphous SiGe layer consists of three main broad bands which are due to TO-mode Si-Si (~465 cm<sup>-1</sup>), Si-Ge (~370 cm<sup>-1</sup>), Ge-Ge (~250 cm<sup>-1</sup>).

#### References:

1. J. Yang, A. Banerjee, and S. Guha, Appl. Phys. Lett. 70, 2975 (1997).
2. M. Lill and B. Schroeder, J. Appl. Phys. 74, 1284 (1999).
3. Q. Wang, E. Iwaniczko, Y. Xu, W. Gao, B. P. Nelson, A. H. Mahan, R. S. Crandall, and H. M. Branz, MRS Spring Meeting Proc. 664, A4.3.1 (2000).
4. R. E. I. Schropp, Y. Xu, E. Iwaniczko, G. A. Zacharias, A. H. Mahan, MRS Symp. Proc. 715, A26.3.1 (2002).
5. S. Klein, F. Finger, R. Carius, B. Rech, L. Houben, M. Luysberg, M. Stutzmann, MRS Symp. Proc. 715, A26.4 (2002).
6. Herry S. Povolny, Doctoral Thesis “Amorphous and Microcrystalline Silicon Photovoltaic Devices Deposited by Hot-wire Chemical Vapor Deposition”, The University of Toledo (USA), March 2003.
7. X. Deng, “High Efficiency and High Rate Deposited Amorphous Silicon-Based Solar Cells”, NREL Phase I Annual Technical Progress Report (Sept. 01, 2001 – Aug. 31, 2002), pp21-26.
8. B. D. Cullity, Elements of X-Ray Diffraction, 2<sup>nd</sup> ed. (Addison-Wesley, Reading, MA, 1978), pp.281-284.